Title

Temporal characterization of fundamental plasma parameters in pulsed liquid electrode plasma (LEP) optical emission spectrometry

Authors

Zhu, Yanbei
Russo, Richard E
Chan, George C-Y

Publication Date

2021-05-01

DOI

10.1016/j.sab.2021.106089

Temporal characterization of fundamental plasma parameters in pulsed liquid electrode plasma (LEP) optical emission spectrometry

Yanbei Zhu[1, 2*], Richard E. Russo[1, 3] and George C.-Y. Chan[1*]

1. Lawrence Berkeley National Laboratory, Berkeley, CA 94720, USA
2. National Institute of Advanced Industrial Science and Technology, 1-1-1 Umezono, Tsukuba, Ibaraki, 305-8563, Japan
3. Applied Spectra, 950 Riverside Pkwy Suite 90, West Sacramento, CA 95605, USA

*Corresponding authors: yb-zhu@aist.go.jp (Y.Zhu); gcchan@lbl.gov (G. Chan)

Abstract

The fundamental characteristics of liquid electrode plasma (LEP), a pulsed plasma source for optical emission spectrometry, were investigated. Two distinct phases were observed during the process of pulsed plasma generation, namely bubble generation and active plasma discharge. The ionization efficiency of the LEP, with Mg as a representative analyte, was gauged from the ratio of Mg II 279.553 nm to Mg I 285.213 nm emission and was found to increase from about 5% to 20% in a close-to-linear fashion with the discharge voltage from 800 V to 1200 V. The Mg II / Mg I ratio of the LEP was 2.5 to 3 orders of magnitude less than that typically offered by an inductively coupled plasma (ICP) but was comparable to other solution-based glow discharges. It was found that an off-time interval of more than 150 ms between successive discharge pulses was required to obtain a stable pulse-to-pulse discharge current. Temporally resolved emissions of Mg II 279.6 nm, Mg I 285.2 nm, Fe I 373.5 nm, OH band head at 306 nm, and Hα line at 656.3 nm showed that the background species (OH band and Hα line) reached their maximum emission intensities at around 0.5 ms to 0.7 ms with respect to the onset of the discharge pulse whereas the maximum emissions were observed between 0.7 ms to 0.9 ms for analyte species (Mg and Fe lines). The electron density observed in the present work was in the range from 5.7×10^{15} cm^{-3} to 8.2×10^{15} cm^{-3}, which was similar to those found in an analytical ICP. The temporal averaged OH rotational temperature was 3300 K, which was comparable to the values of an analytical ICP and solution-based glow discharges. By contrast, the temporally averaged Fe I excitation temperature was around 8900 K, which was even higher than that of an analytical ICP and roughly triple the values obtained by techniques based on glow discharge of liquid samples.

Keywords: liquid electrode plasma optical emission spectrometry; electron number density; ionization efficiency; rotational temperature; excitation temperature

1. Introduction

As one of the trends in the development of analytical techniques for elemental analysis in liquid samples, on-site and low-power-consumption atomic-emission approaches have been studied by multiple research groups. For example, closed and open-air types electrolyte cathode atomic glow discharges (ELCAD) have been presented as candidate techniques for on-line monitoring of trace elements in flowing solution [1, 2]. Liquid-sampling atmospheric-pressure glow discharge (LS-APGD) has been developed to facilitate the analysis of low-volume samples [3, 4]. Solution-cathode glow discharge (SCGD) can be regarded as a modified version of ELCAD with improved stability of optical emission [5, 6]. For both the ELCAD and SCGD, the solution sample to be analyzed serves as one of the discharge electrodes whereas in LS-APGD, the plasma is formed between the surface of the solution exiting a silica capillary housed within a slightly larger capillary and a metallic counter electrode [7]. In all these three techniques, the plasma is operated under *continuous* high voltage of direct current (HVDC) electric power. The typical powers required for these techniques are lower (typically < 100 W) in comparison to the benchmark for atomic emission – the analytical inductively coupled plasma (ICP), which typically operates above 1000 W.

Although these microplasmas are operated at much lower power (by more than one order of magnitude) than the analytical ICP, because of their reduced physical size, power density in these microplasmas in fact is comparable to or even larger than that in the ICP [5, 7]. As such, reported detection limits on selected elements offered by these microplasmas are comparable to or even better than the ICP in some cases [5, 8]. One possible way to further increase the power density is to confine the plasma with a physical barrier. The liquid electrode plasma (LEP) is such a device in that the plasma is confined inside a capillary of micrometer size [9].

Liquid electrode plasma optical emission spectrometry (LEP-OES) is a technique based on atomic emission from a liquid sample loaded in a narrow capillary tunnel between two electrodes, to which *pulsed* HVDC is applied [9]. In its operation, electrically conductive (e.g., acidified) sample solution is loaded into a specially designed solution cell consisting of two liquid reservoirs connected by a micrometer-sized capillary. A metallic electrode is immersed into each reservoir. When a HVDC pulse is applied to the two electrodes, the potential drop and electric field are concentrated inside the micrometer-sized capillary causing solution boiling, bubble creation, and plasma formation inside the capillary [9-11]. Instead of as a continuously operated glow discharge as in ELCAD, LS-APGD, and SCGD, optical emission in LEP-OES is generated by pulsed plasma discharge. Thus, the *active* plasma power of LEP-OES is of a similar order (several 10 W) with those of ELCAD, LS-APGD, and SCGD. However, because the plasma is operated in a pulsed mode, the total energy consumption is greatly reduced. As such, the commercialized version of the LEP offers the option of operation with dry-cell batteries [12]. Partly owing to the commercial availability of LEP-OES instruments, applications reported in recent years include, for example: Na and Li in ZrO_2 sample [9], Au, Pd, Pt in acidic aqueous matrix [13], Cd and Pb in elemental calibrating standards [14], and Cs [15] and Tc [16] in radioactive liquid waste. However, there are only limited reports about the fundamental characterization of this pulsed plasma source [10, 11, 17].

In order to gain a better understanding of the LEP and to obtain stable analytical signals and a higher signal-to-background ratio, we performed fundamental plasma characterization (measurements of excitation temperature, rotational temperature, ionization efficiency, and electron number density) of the LEP in a temporally resolved fashion. As the commercial implementation of the LEP device simply integrates the total optical emission over a series of pulses, it is anticipated that signal-to-background ratio could be improved with temporally resolved detection if the temporal responses of analyte signal and its background are different during the LEP pulse cycle. Accordingly, we also investigated the effect of operating parameters including: solution flow rate, discharge voltage, and discharge off-time interval in-between successive pulses, on the discharge current and its characteristics, and on analyte emission and ionization efficiencies with Mg as the test element.

2. Experimental

2.1 Overview

A commercial pulsed liquid electrode plasma optical emission spectrometer (MH-5000, Micro Emission, Ishikawa, Japan), with in-house modification for trigger signal and current measurement, was used in this work. Figure 1a shows a diagram of the experimental system. The MH-5000 LEP is a self-contained portable instrument equipped with a high-voltage power supply for generating the liquid plasma and an optical spectrometer. Parameters for the pulsed discharge (e.g., voltage, discharge duration, number of discharge cycles, and intervals between consecutive discharges) are all user controllable. Some typical values of operating parameters are: 600 V to 1000 V pulse voltage; 1 ms to 4 ms discharge duration; intervals of 2 ms to 40 ms between consecutive discharges; and 10 to 40 discharge train in a measurement cycle [9, 12, 18-21]. As discussed in detail in other works [9, 10, 13, 14], the LEP is generated inside a custom-made capillary cell located in the instrument. In our case, the capillary cell was made of fused silica. The cross section of the capillary was rectangular and measured 220 μm (width) × 20 μm (depth) with a length of 600 μm. Figure 1b shows a schematic diagram of the capillary and solution channels. Particularly relevant to the present study is the respective solution volume. The volume of the LEP capillary is 0.0026 mm^3, whereas that for the tapered portion joining the capillary and the circular solution channel (i.e., the conical portion) is 0.21 mm^3. Another volume of approximately 2.9 mm^3 is needed to fill the channel up to the surface of the platinum electrode.

The instrument offers two modes of operation – static and continuous solution-flow modes. In both cases, the plasma is operated under constant-voltage mode. In this work, continuous flow analysis was utilized because each measurement consisted of a train of discharge pulses. Only with sample replenishment (i.e., continuous flow) is it reasonable to expect comparatively steady signals for every single discharge and to ensure the reproducibility of plasma for temporal analysis. For this operation, sample solution continuously entered one end of the capillary cell through the designated sample intake port by means of a syringe pump. Excess sample solution was collected through the other end of the cell as waste.

2.2 Spectrometric measurement system

As the objective of this study was to examine the temporal characteristics of the LEP, a gated optical detector was needed. Therefore, we bypassed the built-in optical spectrometer by using a separate optical fiber located close to the capillary where the LEP was formed. The other end of this optical fiber was imaged by a lens onto the entrance slit of an external Czerny-Turner spectrometer with a focal length of 1.25 m (Horiba JY 1250M), coupled with an intensified-CCD (ICCD) detector. A total of four spectral windows centered at around 282 nm for Mg, 311 nm for OH, 374 nm for Fe, and 656 nm for H were sequentially measured. Two gratings, with groove densities of 2400 and 1200 per mm, were used depending on the desired spectral resolution and the width of spectral window that can be captured by the ICCD. The 1200-groove/mm grating was employed for measurement of the Mg and OH windows whereas the 2400-groove/mm grating was used for the Fe and H spectral windows. Furthermore, to balance between spectral resolution and light throughput, slit widths were varied for different spectral windows and were 35 μm for the OH and H windows, 80 μm for the Fe window, and 150 μm for the Mg window. The resultant spectral bandpass ($\Delta\lambda$) was experimentally determined (with a Hg-lamp at nearby wavelengths) to be 18, 30, 40 and 130 pm for the H, Fe, OH and Mg spectral windows, respectively.

Emission intensities from Mg and Fe lines were measured by using samples containing 200 mg L^{-1} Mg and 500 mg L^{-1} Fe, respectively, acidified with 2% w/v HNO_3 (i.e., approximately 0.3 mol L^{-1}). Emission from OH and H were measured with a sample containing 2% HNO_3 only. Depending on the experiment, either temporally integrated or resolved emission was measured. As will be shown later, because emission decays almost instantly once the discharge current ends, the ICCD was set with no gate delay and a gate width identical to the width of the discharge current pulse for measurement of temporal-integrated emission. For temporally resolved measurement, a series of eleven sequential ICCD readings were taken, at each wavelength, at increasing delay times in steps of 0.2 ms, referenced to the trigger signal (see Section 2.3), and with a constant gate width of 0.2 ms.

2.3 Trigger signal for spectrometric detector and measurement of discharge current

For temporally resolved measurement, it is crucial to synchronize the detector with the discharge pulse. Because the MH-5000 instrument is designed for temporally integrated measurements with its built-in spectrometer, it is internally self-triggered with no external trigger option or output. Furthermore, the internal power supply can be controlled only for its voltage output but there is no indication of the discharge current. To understand the temporal emission profile, it is necessary to record the corresponding temporal profile of the discharge current. Therefore, the internal circuitry of the MH-5000 was modified in-house to provide a trigger signal when the electrodes are energized and to allow the measurement of temporal LEP discharge current.

One straightforward approach to tap the circuit for a trigger signal is to exploit the electrical noise associated with an imperfectly shielded, energized high-voltage circuit. When a high-voltage power supply delivers a pulse, an electrical impulse is induced along the conducting wire which usually can be picked up by an open-ended wire placed in close proximity. We collected this impulse by wrapping the electrical wire of the discharge high-voltage power supply with about four rounds of another open-ended wire, termed pick-up wire (see Figure 1a). The other end of this pickup wire was split between a digital oscilloscope for display and recording, and a high-impedance trigger input of a digital delay generator to yield a squared-shaped trigger pulse. Both the width and the amplitude of the triggering pulse from the digital delay generator were user adjustable, and a pulse with 0.1 ms width and +4 V amplitude was somewhat arbitrarily selected to match the ICCD triggering requirement.

To measure current, a resistor of low resistance (11 Ω in our case) was introduced in-series between the power supply and one of the electrodes (see Figure 1a). The LEP current can then be inferred from the voltage drop across this resistor. Figure 2 shows the temporal profile, as measured by a digital oscilloscope, of the voltage across the 11 Ω resistor (related to LEP current), the pick-up wire showing the induced voltage when the power supply was switched on and off, and the trigger pulse for the ICCD.

3. Results and Discussion

3.1 Solution flow rate and number of pulses in a discharge cycle

As the LEP typically operates with pulses each lasting only a few milliseconds, emission from single-pulse LEP is weak. Significant improvement in signal-to-noise ratio can be obtained through signal accumulation from a train of discharge pulses. To facilitate temporal characterization of the plasma, it is desirable to treat each pulse in a discharge cycle as identical and perform signal averaging or integration over repetitive discharge pulses in a cycle. Because each discharge pulse results in “micro-explosions” and the accumulation of thus-generated bubbles may affect the electrical impedance of the sample inside the capillary, continuous flow sample replenishment is needed for reproducible measurements. Even with continuous flow, a delicate balance between solution flow rate and number of pulses in a discharge cycle is needed to produce pulse-to-pulse reproducible discharges. Accordingly, these two factors were first examined and optimized.

A viable way to monitor the pulse-to-pulse reproducibility in a train of LEP discharges is through examining the temporal trace of the current. Standard LEP discharge conditions (1000 V discharge voltage, 2 ms discharge on time, and 2 ms discharge off time) were used and sample solution flow rate was varied from 50 μL min^{-1} to 500 μL min^{-1}. Figure 3 shows three representative temporal discharge-current profiles at flow rates of 100, 200 and 400 μL min^{-1}. For each discharge pulse, the discharge current exhibited an initial spike during the onset of the pulse but then quickly decays to a lower level. At a solution flow of 50 μL min^{-1}, not all discharge pulses showed the initial current spike. At a solution flow rate of 500 μL min^{-1}, because of the narrow discharge capillary, leaking of sample solution through the sample inlet of the instrument, likely as a result of overpressure, was observed. Although none of the studied flow rates gave a perfect train of discharge currents, the pulse-to-pulse discharge current became more comparable to each other as the solution flow rate increased (see Figure 3). In all cases, the first few (about five) pulses always exhibited the largest deviations from the remaining pulses in the discharge train, and the plasma conditions change gradually along the firing sequence. Because the ideal case of identical pulse-to-pulse discharge current could not be established, a compromise was accepted for optimization of solution flow rate. For the discharges from the 6th through 35th pulses, the individual current profiles were similar to each other for sample flow rate at 400 μL min^{-1}. After 40 pulses, the individual current profiles displayed significant shifts. In addition, although there are noticeable differences in the discharge-current profile between the first five pulses and the rest in the train, this difference is comparatively small for 400 μL min^{-1} than in other studied flow rates. Therefore, unless otherwise specified, a sample introduction rate at 400 μL min^{-1} with a train of 30 discharge pulses (to ensure that experiments were performed within the most reproducible pulse-to-pulse regime) was used for subsequent experiments.

The flow-rate dependence is likely related to sample replenishment in the LEP capillary. Generation of the LEP requires solution boiling, bubble creation, and plasma formation inside the capillary [9-11]. In addition, the presence of analyte, H and OH emission indicates (partial) decomposition of the sample electrolyte. As such, compared to *fresh* sample electrolyte, the chemical as well as electrical properties of the *used* electrolyte, defined as the sample solution already subjected to a LEP discharge pulse, are anticipated to be different. With a discharge off time of only 2 ms and a capillary volume of 0.0026 mm^3, a flow rate of 100 μL min^{-1} (i.e., 1.67 mm^3 s^{-1}) is just slightly more than sufficient to flush out and replace the entire *used* sample electrolyte inside the capillary with *fresh* one. At a flow rate of 50 μL min^{-1}, a portion of the used sample remains inside the capillary. In this case, as the chemical property and electrical conductivity of the used sample continue to change and deteriorate during the pulse train, plasma generation starts to fail (i.e., no initial current spike) along the progression of the pulse train. Although the use a flow rate of 100 μL min^{-1} is sufficient to replace all the sample inside the capillary with fresh one during the 2-ms off time, the solution flushed out at the exit of the capillary contains a large fraction of used sample (0.0026/0.0033 = 79%) and with only a small fraction (~21%; this fraction is further reduced if one also accounts for the used sample solution flushed out during the 2-ms plasma-on time) of fresh sample. Because of the narrow bore size of the solution channel, mixing inside the channel is inefficient and the used sample solution likely accumulates at the apex of the conical shaped interface right at the exit of the capillary (see Figure 1b). As a result, pulse-to-pulse discharge current changes (see Figure 3).

The use of a higher solution flow rate not only ensures that the electrolyte inside the capillary is completely replaced with fresh one, but also increases the fraction of fresh-to-used sample at the exit of the capillary, and hence helps to improve the pulse-to-pulse discharge stability. However, even with the maximum studied flow rate of 400 μL min^{-1}, at least 20% of the solution contained in the conical section of the channel (see Figure 1b) is used sample. Therefore, albeit improved, a progressively weakening pulse-to-pulse discharge current was observed even at a flow rate of 400 μL min^{-1}. As will be discussed in Section 3.4, a feasible way to further improve the stability of pulse-to-pulse discharge current is to increase the off-time interval between successive discharge pulses.

3.2 Characteristics of discharge current

Figure 4 depicts the temporal profile of the discharge current in an expanded scale. In agreement with literature [10], there is an initial current spike, which is related to the formation of H_2O bubbles in the solution channel before a plasma can be initiated [11], followed by a comparatively flat current region, which is believed to be the current used to sustain the plasma. As shown in our temporally resolved experiments to be presented in Section 3.5.1, emission from analyte and plasma species was insignificant during the initial current spike. For discussion, the current profile was divided into two zones, and accordingly labeled as the bubble-generation and the active plasma-discharge zones. For many of the measured temporal current profiles, the bubble-generation current quickly dissipated after roughly 0.12 ms from its peak. As a first approximation, the active plasma-discharge current was estimated from the averaged current after 0.12 ms from the current peak till the end of the pulse.

3.3 Estimation of analyte ionization efficiency and effect of discharge voltage

In this section, the effect of discharge voltage and ionization efficiency of a representative analyte – Mg, will be discussed. Figure 5 shows the temporal current profiles as a function of discharge voltages at 600, 700, and 1000 V. At 600 V, not all discharges lead to plasma generation as the bubble-generation current spikes get weaker and disappear after around the 21st pulse. The trapezoidal-shaped current profile after the 24th pulse at 600 V is likely a result of mere electrical conduction through the electrolyte. The bubble and plasma generation, as reflected by the successful generation of the current spike and reproducible active plasma-discharge current, improves as the discharge voltage rises to 700 V and further increases to 1000 V (see Figure 5). As used sample solution, which has different chemical properties and electrical conductivity compared to fresh one, starts to accumulate in-between the electrode and the exit of the discharge capillary, a higher discharge voltage is needed to initiate plasma formation. Figure 6a shows the averaged active plasma-discharge current (i.e., the second zone in Figure 4) and the temporal-integrated Mg II 279.553 nm emission as a function of discharge voltage. The active plasma-discharge current increased linearly from 10 mA to 16 mA with discharge voltage from 800 V to 1200 V. The active plasma current at 700 V is likely an artefact because the current in the second zone of the profile, grows toward the end of the firing sequence (starts to develop at around the 22nd pulse and becomes very clear at the 29th pulse, see Figure 5). This abnormal growth of second-zone current is a sign before the current spike disappears and the whole profile transforms to a trapezoidal shape, as in the case of 18th pulse at 600 V discharge voltage. The temporally integrated Mg II 279.553 nm emission shows a monotonic increasing trend with the voltage. The error bars, which represent the standard deviations of five replicate measurements, are comparatively large and the relative standard deviations range from 14% to 25%. Relative standard deviation between 10 to 20% had been reported by other research groups [12, 15] for LEP-OES.

The spectral window covered by the ICCD is wide enough to include both the Mg II 279.553 nm and the Mg I 285.213 nm lines for each pulse acquisition. The Mg II / Mg I emission ratio is commonly used to gauge plasma robustness [22]. In addition, the Mg II 279 nm / Mg I 285 nm ratio can be readily used to estimate the ionization efficiency, α, of Mg in the plasma through the relationships:

$$\alpha = \frac{n_i^+}{n_{total}} = \frac{n_i^+}{n_i^+ + n_a} = \left(1 + \frac{n_a}{n_i^+}\right)^{-1} \tag{1}$$

$$\begin{aligned}\frac{I_{Mg\,II\,279}}{I_{Mg\,I\,285}} &= \frac{n_i^+}{n_a}\cdot\frac{(gA)_{Mg\,II\,279}}{(gA)_{Mg\,I\,285}}\cdot\frac{\lambda_{Mg\,I\,285}}{\lambda_{Mg\,II\,279}}\cdot\frac{Q_{Mg\,I}}{Q_{Mg\,II}}\cdot\exp\left(\frac{-E^{exc}_{Mg\,II\,279}+E^{exc}_{Mg\,I\,285}}{kT_{exc}}\right)\\ &\approx 0.721\times\frac{1}{2}\times\frac{n_i^+}{n_a}\end{aligned}\tag{2}$$

where n_i^+, n_a and n_{total} represent the number densities of singly charged Mg ions, neutral Mg atoms, and the sum of Mg ions and atoms, respectively; I, g, A, λ, Q, E^{exc} are respectively the emission intensity, degeneracy of the upper transition state, transition probability, wavelength, partition function and excitation potential of the Mg emission line or ionization state denoted in the subscript; k and T_{exc} are the Boltzmann constant and the excitation temperature, respectively. Because the excitation potentials of these two Mg lines are very close (4.434 eV for Mg II 279.553 nm and 4.346 eV for Mg I 285.213 nm [23]), the exponential term in Equation 2 is insensitive to a change in excitation temperature and is very close to unity. The Mg II 279 nm / Mg I 285 nm emission ratio is dominated by the ionization efficiency of Mg in the plasma. The spectroscopic-constant factor (i.e., g, A and λ) is 0.721 [23] for this pair of Mg lines and the ratio of Mg I partition function to that of Mg II can be approximated as 1:2.

Through the well-known relationship among power, voltage and current, the average active plasma-discharge power as a function of discharge voltage can be evaluated. Figure 6b presents the active discharge power and Mg ionization efficiency. The Mg ionization efficiency increases from about 5% to 20% in a close-to-linear fashion with the discharge voltage from 800 V to 1200 V. The estimated active discharge power ranged from 8 W to 19 W. A good correlation between Mg ionization efficiency and active discharge power was found.

Table 1 compares the Mg II 279.533 nm / Mg I 285.213 nm ratio and Mg ionization efficiency of different analytical plasmas [8, 24-34]. It is common to use either the Mg II 279.533 nm, or another Mg II line that belongs to the same multiplet at 280.270 nm, for the calculation of the Mg II / Mg I ratio. In cases that the Mg II / Mg I ratio was presented based on Mg II 280.270 nm, a multiplication by a factor of 2 would transform the ratio to the one based on Mg II 279.533 nm. Among the most common spectrochemical plasma or discharge sources (see Table 1), the Mg II / Mg I ratio of the LEP ranks low and is 2.5 to 3 orders of magnitude less than that typically offered by an ICP [34]. However, the Mg II / Mg I ratio of the LEP is quite comparable to those sources in which the plasma or discharge is in direct contact with excessive solution samples, like the solution cathode glow discharge (SCGD) [8, 24] or the atmospheric pressure glow discharge (APGD) in contact with liquid [25, 26].

3.4 Optimization of off-time interval between successive discharge pulses for stable pulse-to-pulse discharge current

Although the use of 400 μL min^{-1} sample solution flow rate and limiting the number of discharge pulses to 30 in one cycle help to improve pulse-to-pulse reproducibility as demonstrated in Figure 3, a progressively weakening discharge current was measured. Specifically, the plasma conditions of the first few pulses are dissimilar from the rest, which introduces uncertainties if each pulse is treated as an individual repetitive measurement. With an ICCD detector, temporally resolved measurements can be achieved only through repetitive discharge firings and integration from multiple, ideally reproducible, discharge events. As such, a study was performed to identify the operating parameters that can further improve the pulse-to-pulse discharge current profile. It was found that by increasing the off-time interval between successive discharge pulses, the current profile of individual firing is more reproducible throughout the discharge train.

Figure 7a shows the measured temporal discharge current for a train of pulses with off-time of 2 ms and 64 ms between successive firings. In both cases, the discharge-on time was 2 ms. Discharge current for all the 30 pulses, in a similar format as those presented in Figure 5, were continually measured. However, because of the different off-time between successive firings, it would be easier to extract individual current pulse from the train for comparison. Furthermore, for clarity, only the current profiles of the 1st, 3rd, 6th, 10th, 15th, 20th, and 25th discharges were shown in the figure. The current profiles of the first pulse with off-time of 2 ms and 64 ms were found to be similar. However, depending on the off-time interval between successive discharges (2 ms *vs.* 64 ms), the current profiles were dramatically different even for the third pulse in the train. With an off-time interval of 2 ms, the current profile of the third pulse was already noticeably different from that of the first pulse, whereas the third-pulse profile taken with an off-time interval of 64 ms shared some resemblance with that of its first pulse (see Figure 7a). Because the whole system (sample reservoirs, channels, and capillary) is filled with wholly fresh sample for the first LEP pulse, it is used as a comparison standard here. In the ideal case in which discharge current is reproducible on a pulse-to-pulse basis, all subsequent pulses in a train should exhibit a similar temporal profile as the first pulse. For later pulses in the train (i.e., 6th pulse and beyond), the current profile were remarkably different than that of the first pulse for the case with an off-time interval of 2 ms. On the other hand, although a decreased plasma-discharge zone was also observed for 64-ms off-time interval, the current was appreciably larger. Thus, increasing the off-time interval between successive firings facilitates a more stable and reproducible pulse-to-pulse discharge.

Although increasing the off-time interval between successive discharges to 64 ms improves pulse-to-pulse stability, a non-negligible decrease in current was still observed for later pulses in the train, indicating that a longer off-time is needed. To optimize the off-time interval, a simplified approach based on the averaged temporal profile of discharge current from all thirty individual pulses in a discharge train is used here. Figure 7b shows the temporal profile of discharge current of the *first* pulse as a function of off-time interval between successive pulses. The current spikes for bubble generation vary but should not be a primary concern; the main focus should be on the active plasma current. As expected, the off-time interval is ineffective for the first pulse. The temporal profiles of active plasma current (i.e., the second zone in Figure 4) of the *first* pulse are comparable for a wide range of off-time intervals. Also shown in Figure 7b is the averaged temporal profile for the first pulse.

A reproducible pulse-to-pulse discharge train is the one in which the temporal profile of the active plasma current of *all* pulses in the train are similar to that of the first pulse; otherwise, a decreasing trend in discharge current would be observed as the train progresses (see Figure 7a). Therefore, it is convenient to use the current profile of the *first* pulse as the comparison benchmark. Only under a relatively reproducible pulse-to-pulse condition, the *averaged* temporal profile of *all* the thirty individual pulses in a discharge train is similar to that of the *first-pulse* reference. If there is a decreasing drift in the discharge current, the *averaged* temporal profile would then be smaller than that of the *first-pulse* reference.

Figure 7c shows the averaged temporal profile of discharge current from *all* thirty individual pulses in a discharge train as a function of off-time interval between successive pulses. Also depicted in Figure 7c is the averaged temporal profile of discharge current of the *first* pulse (see Figure 7b). Non-linear and gradual increase was observed for the average active-discharge current with the increase of off-time interval, i.e., the longer the off-time interval, the stronger the discharge current. As shown in Figure 7c, the average discharge current profiles with off-time intervals of 150 ms and 200 ms are similar to that of the *first-pulse* reference. Considering that 200 ms was the upper limit for off-time interval setting in the present instrument, 150 ms was chosen for off-time interval in the experiments on temporal resolved plasma LEP-OES diagnostics described below. For a solution flow rate of 400 μL min^{-1} and assuming a laminar solution-flow pattern, it requires less than 0.5 ms to flush out used sample from the discharge capillary but about 460 ms to completely replace the sample solution in-between the capillary and the electrode surface. The data presented in Figure 7c and the finding that the LEP system needs 150 ms for comparatively stable pulse-to-pulse operation (a considerable fraction compared to the 460 ms required for complete sample-solution replacement) suggest that the used sample solution has a detrimental effect on the plasma generation.

With an off-time interval between successive discharge pulses of 150 ms, the temporally averaged LEP-discharge *active* current (i.e., the second zone after the spike) was estimated to be 54 mA, giving an estimated active LEP power of 54 W (with 1000 V discharge voltage). The active LEP power is comparable to other solution-based microplasmas, for example, the SCGD and the LS-APGD. Typical operating powers for the SCGD and LS-APGD are in the range of 60-80 W [35-37] and < 50 W [27, 38], respectively.

3.5 Temporally resolved plasma diagnostics on LEP-OES

3.5.1 Temporal discharge current and emission characteristics

Temporally resolved plasma emission and plasma fundamental parameters (e.g., electron density by Hα Stark broadening, Mg ionization efficiency, OH rotational temperature, and Fe I excitation temperature) were investigated. The ICCD was set with a gate width of 0.2 ms to measure the temporal emission of the LEP. A total of eleven gate delays were used to cover the temporal emission profiles from 0.0 ms to 2.2 ms with respect to the trigger pulse. Figure 8a shows the temporal profile of the discharge current (black line), its division into the eleven gates, and the averaged discharge current (red circle symbol) within each gate lasting 0.2 ms. With the exception of the first two gates which overlap with the current spike at the onset of the discharge, the average current in each gate well represents the corresponding discharge current. The center of the gate is used to indicate the time of the discharge cycle (i.e., a gate with delay of 0.0 ms was active from 0.0 ms to 0.2 ms, and thus was labeled as 0.1 ms).

In addition to the discharge current profile, Figure 8b shows the temporally resolved emission from five species – Mg I 285.2 nm, Mg II 279.6 nm, Fe I 373.5 nm, OH bandhead at 306 nm, and Hα line at 656.3 nm. Each temporal emission profile was normalized to its total (i.e., temporal integrated) emission intensity. The lines connecting the data points are for sight guidance only. Both Mg I and Mg II emission were absent in the first 0.2 ms of the pulse (i.e., during the current spike) and appeared at 0.3 ms (window from 0.2 ms to 0.4 ms). The Mg signals attained their maxima at ~ 0.9 ms. Weak Mg emission was still measurable immediately after the discharge pulse was turned off (at 2.1 ms). Despite the much higher current spike at the onset of the discharge, virtually no analyte and background (H and OH) emission were observed in the first gate. The absence of strong emission during the first 0.2 ms supports the assertion mentioned above that the initial current spike is responsible for bubble formation prior to plasma formation.

There is a subtle difference between emission profiles of the analytes (Mg and Fe) and the background-species (OH and H). Overall, the analyte emission peaks at around 0.7 ms to 0.9 ms whereas that from background species was at 0.5 to 0.7 ms. It appeared that the peak of Fe I emission shifted slightly earlier to 0.7 ms; however, the difference between the peak appearance time of Fe and Mg emission was subtle and was within experimental uncertainty. Molecular OH emission peaked at around 0.7 ms and the Hα line attained its maximum slightly earlier at 0.5 ms to 0.7 ms. The fact that it takes at least 0.5 ms for the background species to reach their emission maxima (and slightly longer for the analyte species) suggests that discharge pulses shorter than 0.5 ms are probably not effective for LEP.

3.5.2 Temporally resolved electron number density and Mg ionization efficiency

Figure 9 shows the temporally resolved electron number density and ionization efficiency, which were determined from the Stark broadening of the Hα line with the full-width-at-half-area (FWHA) approach [39] and the Mg II / Mg I emission-intensity ratio as outlined in Equation 2, respectively. As remarked by Gigosos *et al.* [39], for electron-density measurements with the Hα line, the FWHA approach is better than the full-width-at-half-maximum (FWHM) method because the latter, albeit simpler in procedure, exhibits strong dependence on electron temperature whereas the temperature dependence of the FWHA method is much weaker. Electron density exhibits a temporally decreasing trend. As can be seen from Figure 9, the highest electron number density was found at 0.3 ms, the first gate in which adequate and reliable Hα emission could be measured. The variation of electron density is comparatively small over the discharge period. On an absolute basis, the electron density is regarded as high for a microplasma and varied between 5.7×10^{15} cm^{-3} and 8.2×10^{15} cm^{-3}. Such values for electron density are similar to those found in an analytical ICP [40, 41]. For comparison, the reported electron density for the SCGD and the LS-APGD are in the range of 3×10^{14} to 9×10^{14} cm^{-3} [24] and 2.8×10^{15} cm^{-3} [42], respectively.

The Mg II 279 nm / Mg I 285 nm ratios were relatively narrow and between 0.09 and 0.14 over this time duration. The calculated ionization efficiency of Mg ranged between 21% and 28%. The Mg II / Mg I ratio (and hence, Mg ionization efficiency) attained its maximum at ~ 0.9 ms which coincided with the maxima of Mg emission, and then slowly declined (see Figure 9).

3.5.3 Temporally resolved rotational and excitation temperatures

Temporal profiles of OH rotational and Fe I excitation temperatures in the LEP also were determined. Seven rotational levels of the Q_1-branch of the OH $A\,^2\Sigma^+ - X\,^2\Pi$ band and a set of seven Fe I emission lines with excitation potentials spanning from 3.332 eV to 4.301 eV were used as probes for rotational and excitation temperatures, respectively. Both temperatures were determined through the well-established Boltzmann-plot method as detailed elsewhere [43]. Figures 10a and 10b show the measured emission spectra of the OH rotational features and the Fe I emission lines used for the temperature determinations, respectively. These data, once again, illustrate the lack of measurable emission from analyte and background-species during the initial spike of the discharge current (delay time zero with ICCD detector gate from 0.0 ms to 0.2 ms).

Figure 11 shows the measured rotational and excitation temperatures. All Boltzmann plots are linear with correlation coefficients better than 0.990 for OH rotational temperature (with the exception of the data point at 2.1 ms, which was measured immediately after the cutoff of the discharge current, with a coefficient of 0.980) and better than 0.992 for the Fe I excitation temperature. Within experimental uncertainties, both the OH and Fe I temperatures showed no variation with delay time. The temporal averaged OH and Fe I temperatures were 3300 K and 8900 K, respectively. The Fe I excitation temperature of a LEP was also investigated by Kumai and Takamura [11], and a range between 6200 K and 8600 K was reported, depending on the operating conditions as well as the material used to fabricate the capillary cell. With Cu as the thermometric species, excitation temperature of 8000 K was reported [10].

The OH rotation temperature of the LEP is similar to that of the other solution-based discharges. The OH temperature for a SCGD was reported to be fairly constant at roughly 3000 K throughout most of the discharge and increased to 3500 K close to the negative glow and the cathode [6]. For LS-APGD, depending on the powering geometries and sheath gas composition, the OH rotational temperature ranged from 2100 K to 2600 K with N_2 as the sheath gas and increased to 2300 K to 3000 K with He as the sheath gas [44]. In fact, even for a plasma as high power as the analytical ICP, the OH rotational temperature is in the vicinity of 3000 K. For example, Novotny *et al.* [34] studied the OH temperature in an ICP operated under a range of experimental conditions and water loadings and reported a relatively narrow range between 2400 K and 3800 K.

In contrast, the Fe I excitation temperature of the LEP at ~ 9000 K is high compared to other solution-based discharges or even the analytical ICP. For SCGD, the Fe I excitation temperature ranged from 2500 K at the anodic edge of the positive column to 5000 K towards the negative glow [6]. The Fe I temperature for the LS-APGD were between 2400 K to 3100 K and 2600 K to 3600 K, respectively, with N_2 and He as the sheath gas [44]. For a range of operating conditions and water loadings in an ICP, the reported Fe I temperature varied between 5500 K to 6400 K [34].

4. Conclusion

In this study, the physical plasma conditions of the LEP operated beyond the typical operating conditions as recommended by the instrument vendor was characterized in a temporally resolved fashion. Temporally resolved plasma diagnostics of the LEP were investigated through an in-house built trigger system based on picking up the induced electrical impulse when the high-voltage supply was energized. We found that long off-time interval (at least 64 ms, and preferably ≥ 150 ms) between successive discharge pulses was crucial for reproducible pulse-to-pulse discharge-current behavior. Long off-time interval also offered higher active discharge power and a more robust plasma. The necessity to use a long off-time interval is related to the altered chemical and electrical properties of the sample solution after its exposure to the LEP. A relatively long off-time interval and high solution flow rate are needed to flush the used sample solution not only out of the narrow LEP capillary, but also the volume in-between the capillary exit and the electrode. It is somewhat surprising to note the detrimental effect on LEP generation that the used sample solution could bring to subsequent discharge pulses. An implication of this finding is that solution-flowing mode should be used over static mode whenever possible.

Results from the temporally resolved plasma characterization demonstrate that discharge pulses shorter than 0.5 ms were inefficient for analytical LEP-OES. Temporal profile of the discharge current can be divided into two distinct zones – an initial spike followed by a relatively steady active discharge current. No analyte and background (H and OH) emission was observed during the current spike, which is related to bubble formation in the solution prior to plasma formation. The overall analyte emission and ionization efficiency were found to correlate with the current in the active plasma-discharge region. Like any analytical plasma, the kinetics of plasma physical processes (desolvation, atomization, excitation, ionization) are important, and it takes about 0.7 ms to 0.9 ms for the emission from different analyte species to attain their maxima. Thus, the overall emission efficiency would be discounted if short discharge pulses were utilized.

Acknowledgements

Work from Lawrence Berkeley National Laboratory was partly supported by the US Department of Energy, Office of Defense Nuclear Nonproliferation Research and Development, under contract number DE-AC02-05CH11231 at the LBNL.

Table 1 Comparison of the Mg II 279.553 nm / Mg I 285.213 nm ratio (plasma robustness) and estimated Mg ionization efficiency of different types of microplasma and laboratory-based analytical plasma.

Source	Description	$\frac{\text{Mg II 279.6 nm}}{\text{Mg I 285.2 nm}}$	Ionization Efficiency†	Ref.
Microplasma in contact with sample solution in excess:				
Liquid Electrode Plasma (LEP)	Standard conditions: 2 ms off-time interval, 700 V to 1200 V, 2 ms plasma on-time, 8 W to 19 W active plasma power	0.0182 (700 V) – 0.0897 (1200 V)	4.8% (700 V) – 20% (1200 V)	This work
Liquid Electrode Plasma (LEP)	Extended off-time condition: 150 ms off-time interval, 1000 V, 2 ms plasma on-time, 54 W active plasma power	0.09 – 0.14 (temporal)	21% – 28% (temporal)	This work
Solution Cathode Glow Discharge (SCGD)	3 mm electrode gap, 75 mA, ~1050 V [6]	0.0263 (negative glow) 0.0171 (positive column)	6.8% (negative glow) 4.5% (positive column)	[24]
Solution Cathode Glow Discharge (SCGD)	New design of electrode arrangement; 3 mm electrode gap, 65 mA, 1000 V	0.04*	10%	[8]
Direct current Atmospheric Pressure Glow Discharge (APGD) in contact with liquid	Electrode gap 2.5 mm, 20 mA, 1500 V, forward power 30 W.	0.035	8.8%	[25]
Direct current Atmospheric Pressure Glow Discharge (APGD) in contact with liquid	20 mA, 1100 V to 1700 V, electrode gap 0.5 mm to 4.0 mm	0.027 – 0.080	9 – 21%‡	[26]
Other microplasma; total consumption of sample solution:				
Liquid Sampling-Atmospheric Pressure Glow Discharge (LS-APGD)	60 mA, voltage not reported but < 2 kV	1.2	77%	[27]

Other laboratory-based analytical plasma:				
Nitrogen Microwave-Induced Plasma (MIP)	Okamoto cavity; 1200 W microwave power	0.6 – 5.2* (observation height dependent)	62% – 94%	[28]
Nitrogen Microwave-Induced Plasma (MIP)	Hammer cavity; 1000 W microwave power	0.52 – 4.02* (observation position and nebulizer gas flow dependent)	59% – 92%	[29]
Nitrogen Microwave-Induced Plasma (MIP)	Hammer cavity; 1000 W microwave power	0.74 (0.7 L/min nebulizer flow) – 1.24* (0.5 L min^{-1})	67% – 77%	[30]
Microwave driven ICP (MICP)	250 W – 300 W microwave power	1.8 (Ring washer coupler MICP) 3.4 (Multi helix coupler MICP)	83% (Ring washer coupler MICP) 90% (Multi helix coupler MICP)	[31]
Microwave-sustained, Inductively Coupled Atmospheric-pressure Plasma (MICAP)	1500 W microwave power (magnetron); nitrogen MIP	3.6 – 3.8*	91%	[32]
Atmospheric pressure Parallel Plate Capacitively Coupled Plasma (PP-CCP)	Dry sample introduction with electrothermal vaporization; forward power 50 W – 300 W	0.16 – 1.15	36 – 83%‡	[33]
Inductively Coupled Plasma (ICP)	Argon ICP, various conditions (power, solvent loading, and observation heights)	16 – 32* (robust plasma) 2 – 16* (non-robust plasma)	98% – 99% (robust plasma) 85% – 98% (non-robust plasma)	[34]

*Original Mg II / Mg I ratio was reported with the Mg II 280.270 nm line and was transformed to Mg II 279.553 nm through multiplication with a conversion factor of 2.

†Unless otherwise noted, all Mg ionization efficiencies were estimated with Equation 2.

‡Ionization efficiency directly quoted from reference.

Figure Captions

Figure 1 (a) Schematic diagram of the in-house modified system for temporal characterization of fundamental plasma parameters in a pulsed LEP-OES. (b) Schematic diagram (top view, not drawn to scale) of solution flow inside the LEP setup. The estimated volume of the LEP capillary, conical interface, and channel (up to electrode surface) are 0.0026 mm^3, 0.2 mm^3 (for each side) and 2.9 mm^3 (for each side), respectively.

Figure 2 Representative signals obtained for the discharge current through the 11 Ω resistor, pick-up wire, and trigger pulse for ICCD (Sample introduction: 400 μL min^{-1}; high voltage for LEP: 1000 V; test sample: Mg 200 mg L^{-1} acidified with 2% v/v HNO_3). The traces are offset from each other for clarity.

Figure 3 Dependence of temporal current profiles on the flow rates of sample introduction (LEP conditions: 1000 V, pulse-on time: 2 ms, off-time interval: 2 ms; test sample: Mg 200 mg L^{-1} acidified with 2% v/v HNO_3).

Figure 4 Expanded view of discharge current temporal profile showing two distinct components – an initial current spike related to the generation of the bubble prior to plasma formation, and a comparatively flat current region after the spike for sustentation of the plasma.

Figure 5 Dependence of the temporal current profiles on discharge voltages (Sample introduction: 400 μL min^{-1}; pulse-on time: 2 ms, off-time interval: 2 ms; test sample: Mg 200 mg L^{-1} acidified with 2% v/v HNO_3).

Figure 6 Effects of LEP discharge voltage on (a) averaged active discharge current (i.e., the second zone in Figure 4) and temporally integrated Mg II emission, and (b) averaged active discharge power and Mg ionization efficiency. Error bars represent the standard deviations from five replicated emission measurements.

Figure 7 Dependence of pulse-to-pulse discharge-current stability on off-time interval between successive discharge pulses. (a) The measured temporal profiles of discharge current from selected firings out of a train of 30 discharge pulses with off-time of 2 ms and 64 ms between successive firings. In both cases, the discharge-on time was 2 ms. (b) The temporal profile of discharge current of the *first* pulse (and their average) with different off-time interval settings. (c) The averaged temporal profile of discharge current (n = 30) as a function of off-time interval between successive pulses. The averaged profile of the *first* pulse serves as the comparison benchmark.

Figure 8 Signal profiles for temporal discharge current and temporal optical emission. (a) The temporal current profile (black line), the division of the discharge into eleven gates, and the averaged discharge current (red dots) within each gate lasting 0.2 ms. (b) The temporal resolved emission from five species – Mg I 285.2 nm, Mg II 279.6 nm, Fe I 373.5 nm, OH bandhead at 306 nm, and Hα line at 656.3 nm. LEP conditions: 1000 V discharge voltage, 2 ms discharge on time, 150 ms discharge off time, 30 pulses in a discharge train, 54 W estimated active-plasma power.

Figure 9 The temporal resolved ionization efficiency of Mg and electron number density of the LEP.

Figure 10 Representative emission spectra for evaluation of temporal resolved (a) OH rotational temperature, and (b) Fe I excitation temperature. The selected spectral features used for the Boltzmann plot are as marked.

Figure 11 The temporal resolved OH rotational and Fe I excitation temperatures of the LEP.

References

1. T. Cserfalvi, P. Mezei, Direct solution analysis by glow discharge: Electrolyte-cathode discharge spectrometry, J. Anal. At. Spectrom. 9 (1994) 345-349.
2. H.J. Kim, J.H. Lee, M.Y. Kim, T. Cserfalvi, P. Mezei, Development of open-air type electrolyte-as-cathode glow discharge-atomic emission spectrometry for determination of trace metals in water, Spectrochim. Acta Part B 55 (2000) 823-831.
3. R.K. Marcus, W.C. Davis, An atmospheric pressure glow discharge optical emission source for the direct sampling of liquid media, Anal. Chem. 73 (2001) 2903-2910.
4. W.C. Davis, R.K. Marcus, An atmospheric pressure glow discharge optical emission source for the direct sampling of liquid media, J. Anal. At. Spectrom. 16 (2001) 931-937.
5. M.R. Webb, F.J. Andrade, G.M. Hieftje, Compact glow discharge for the elemental analysis of aqueous samples, Anal. Chem. 79 (2007) 7899-7905.
6. M.R. Webb, F.J. Andrade, G. Gamez, R. McCrindle, G.M. Hieftje, Spectroscopic and electrical studies of a solution-cathode glow discharge, J. Anal. At. Spectrom. 20 (2005) 1218-1225.
7. R.K. Marcus, B.T. Manard, C.D. Quarles, Liquid sampling-atmospheric pressure glow discharge (LS-APGD) microplasmas for diverse spectrochemical analysis applications, J. Anal. At. Spectrom. 32 (2017) 704-716.
8. T.A. Doroski, A.M. King, M.P. Fritz, M.R. Webb, Solution–cathode glow discharge – optical emission spectrometry of a new design and using a compact spectrograph, J. Anal. At. Spectrom. 28 (2013) 1090-1095.
9. M. Banno, E. Tamiya, Y. Takamura, Determination of trace amounts of sodium and lithium in zirconium dioxide (ZrO_2) using liquid electrode plasma optical emission spectrometry, Anal. Chim. Acta 634 (2009) 153-157.
10. Y. Kohara, Y. Terui, M. Ichikawa, T. Shirasaki, K. Yamamoto, T. Yamamoto, Y. Takamura, Characteristics of liquid electrode plasma for atomic emission spectrometry, J. Anal. At. Spectrom. 27 (2012) 1457-1464.
11. M. Kumai, Y. Takamura, Excitation temperature measurement in liquid electrode plasma, Jpn. J. Appl. Phys. 50 (2011) 096001.
12. T. Yamamoto, I. Kurotani, A. Yamashita, J. Kawai, S. Imai, Elemental analysis of leaching solution from soils in the mountain district of Shikoku with a handy-type liquid electrode plasma atomic emission spectrometer, Bunseki Kagaku 59 (2010) 1125-1131.
13. S. Barua, I.M.M. Rahman, M. Miyaguchi, A.S. Mashio, T. Maki, H. Hasegawa, On-site analysis of gold, palladium, or platinum in acidic aqueous matrix using liquid electrode plasma-optical emission spectrometry combined with ion-selective preconcentration, Sens. Actuators B Chem. 272 (2018) 91-99.
14. A. Kitano, A. Iiduka, T. Yamamoto, Y. Ukita, E. Tamiya, Y. Takamura, Highly sensitive elemental analysis for Cd and Pb by liquid electrode plasma atomic emission spectrometry with quartz glass chip and sample flow, Anal. Chem. 83 (2011) 9424-9430.
15. V.-K. Do, M. Yamamoto, S. Taguchi, Y. Takamura, N. Surugaya, T. Kuno, Quantitative determination of total cesium in highly active liquid waste by using liquid electrode plasma optical emission spectrometry, Talanta 183 (2018) 283-289.
16. M. Yamamoto, V.-K. Do, S. Taguchi, T. Kuno, Y. Takamura, Spectrochemistry of technetium by liquid electrode plasma optical emission spectrometry and its applicability of quantification for highly active liquid waste, Spectrochim. Acta Part B 155 (2019) 134-140.

17. P. Ruengpirasiri, P.T. Tue, H. Miyahara, A. Okino, Y. Takamura, Study on effect of introduced gas bubbles for the low channel damage in direct and alternating current liquid electrode plasma atomic emission spectrometry, Jpn. J. Appl. Phys. 58 (2019) 097001.
18. M. Kumai, K. Nakayama, Y. Furusho, T. Yamamoto, Y. Takamura, Quantitative determination of lead in soil by solid-phase extraction/liquid electrode plasma atomic emission spectrometry, Bunseki Kagaku 58 (2009) 561-567.
19. K. Nakayama, T. Yamamoto, N. Hata, S. Taguchi, Y. Takamura, Liquid electrode plasma atomic emission spectrometry combined with multi-element concentration using liquid organic ion associate extraction for simultaneous determination of trace metals in water, Bunseki Kagaku 60 (2011) 515-520.
20. S. Kagaya, S. Nakada, Y. Inoue, W. Kamichatani, H. Yanai, M. Saito, T. Yamamoto, Y. Takamura, K. Tohda, Determination of cadmium in water samples by liquid electrode plasma atomic emission spectrometry after solid phase extraction using a mini cartridge packed with chelate resin immobilizing carboxymethylated pentaethylenehexamine, Anal. Sci. 26 (2010) 515-518.
21. S. Barua, I.M.M. Rahman, I. Alam, M. Miyaguchi, H. Sawai, T. Maki, H. Hasegawa, Liquid electrode plasma-optical emission spectrometry combined with solid-phase preconcentration for on-site analysis of lead, J. Chromatogr. B 1060 (2017) 190-199.
22. J.M. Mermet, Use of magnesium as a test element for inductively coupled plasma atomic emission spectrometry diagnostics, Anal. Chim. Acta 250 (1991) 85-94.
23. A. Kramida, Y. Ralchenko, J. Reader, NIST ASD Team, NIST atomic spectra database (ver. 5.7.1) [online], National Institute of Standards and Technology, Gaithersburg, MD, https://physics.nist.gov/asd, (accessed 3 May 2020).
24. M.R. Webb, G.C.Y. Chan, F.J. Andrade, G. Gamez, G.M. Hieftje, Spectroscopic characterization of ion and electron populations in a solution-cathode glow discharge, J. Anal. At. Spectrom. 21 (2006) 525-530.
25. P. Jamróz, P. Pohl, W. Żyrnicki, An analytical performance of atmospheric pressure glow discharge generated in contact with flowing small size liquid cathode, J. Anal. At. Spectrom. 27 (2012) 1032-1037.
26. P. Jamróz, W. Żyrnicki, Spectroscopic characterization of miniaturized atmospheric-pressure dc glow discharge generated in contact with flowing small size liquid cathode, Plasma Chem. and Plasma Proc. 31 (2011) 681-696.
27. B.T. Manard, J.J. Gonzalez, A. Sarkar, X. Mao, L.X. Zhang, S. Konegger-Kappel, R.K. Marcus, R.E. Russo, Investigation of spectrochemical matrix effects in the liquid sampling-atmospheric pressure glow discharge source, Spectrochim. Acta Part B 100 (2014) 44-51.
28. Z. Zhang, K. Wagatsuma, Matrix effects of easily ionizable elements and nitric acid in high-power microwave-induced nitrogen plasma atomic emission spectrometry, Spectrochim. Acta Part B 57 (2002) 1247-1257.
29. D.A. Goncalves, T. McSweeney, G.L. Donati, Characteristics of a resonant iris microwave-induced nitrogen plasma, J. Anal. At. Spectrom. 31 (2016) 1097-1104.
30. N. Chalyavi, P.S. Doidge, R.J.S. Morrison, G.B. Partridge, Fundamental studies of an atmospheric-pressure microwave plasma sustained in nitrogen for atomic emission spectrometry, J. Anal. At. Spectrom. 32 (2017) 1988-2002.
31. J. Giersz, K. Jankowski, A. Ramsza, E. Reszke, Microwave-driven inductively coupled plasmas for analytical spectroscopy, Spectrochim. Acta Part B 147 (2018) 51-58.

32. K.M. Thaler, A.J. Schwartz, C. Haisch, R. Niessner, G.M. Hieftje, Preliminary survey of matrix effects in the microwave-sustained, inductively coupled atmospheric-pressure plasma (MICAP), Talanta 180 (2018) 25-31.
33. M.M. Rahman, M.W. Blades, Ionization of Mg and Cd in an atmospheric pressure parallel plate capacitively coupled plasma, J. Anal. At. Spectrom. 15 (2000) 1313-1319.
34. I. Novotny, J.C. Farinas, J.L. Wan, E. Poussel, J.M. Mermet, Effect of power and carrier gas flow rate on tolerance to water loading in inductively coupled plasma atomic emission spectrometry, Spectrochim. Acta Part B 51 (1996) 1517-1526.
35. C.G. Decker, M.R. Webb, Measurement of sample and plasma properties in solution-cathode glow discharge and effects of organic additives on these properties, J. Anal. At. Spectrom. 31 (2016) 311-318.
36. A.J. Schwartz, S.J. Ray, E. Elish, A.P. Storey, A.A. Rubinshtein, G.C.Y. Chan, K.P. Pfeuffer, G.M. Hieftje, Visual observations of an atmospheric-pressure solution-cathode glow discharge, Talanta 102 (2012) 26-33.
37. A.J. Schwartz, S.J. Ray, G.C.Y. Chan, G.M. Hieftje, Spatially resolved measurements to improve analytical performance of solution-cathode glow discharge optical-emission spectrometry, Spectrochim. Acta Part B 125 (2016) 168-176.
38. H.W. Paing, K.A. Hall, R.K. Marcus, Sheathing of the liquid sampling – atmospheric pressure glow discharge microplasma from ambient atmosphere and its implications for optical emission spectroscopy, Spectrochim. Acta Part B 155 (2019) 99-106.
39. M.A. Gigosos, M.A. Gonzalez, V. Cardenoso, Computer simulated Balmer-alpha, -beta and -gamma Stark line profiles for non-equilibrium plasmas diagnostics, Spectrochim. Acta Part B 58 (2003) 1489-1504.
40. M. Huang, S.A. Lehn, E.J. Andrews, G.M. Hieftje, Comparison of electron concentrations, electron temperatures, gas kinetic temperatures, and excitation temperatures in argon ICPs operated at 27 and 40 MHz, Spectrochim. Acta Part B 52 (1997) 1173-1193.
41. P.E. Walters, W.H. Gunter, P.B. Zeeman, Electron density characterization of 27.1 and 50 MHz inductively coupled plasmas by means of Abel corrected Stark broadened Hβ line profiles, Spectrochim. Acta Part B 41 (1986) 133-141.
42. B.T. Manard, J.J. Gonzalez, A. Sarkar, M.R. Dong, J. Chirinos, X.L. Mao, R.E. Russo, R.K. Marcus, Liquid sampling-atmospheric pressure glow discharge as a secondary excitation source: Assessment of plasma characteristics, Spectrochim. Acta Part B 94-95 (2014) 39-47.
43. C. Engelhard, G.C.Y. Chan, G. Gamez, W. Buscher, G.M. Hieftje, Plasma diagnostic on a low-flow plasma for inductively coupled plasma optical emission spectrometry, Spectrochim. Acta Part B 63 (2008) 619-629.
44. W.C. Davis, R.K. Marcus, Role of powering geometries and sheath gas composition on operation characteristics and the optical emission in the liquid sampling-atmospheric pressure glow discharge, Spectrochim. Acta Part B 57 (2002) 1473-1486.

Figure 1a

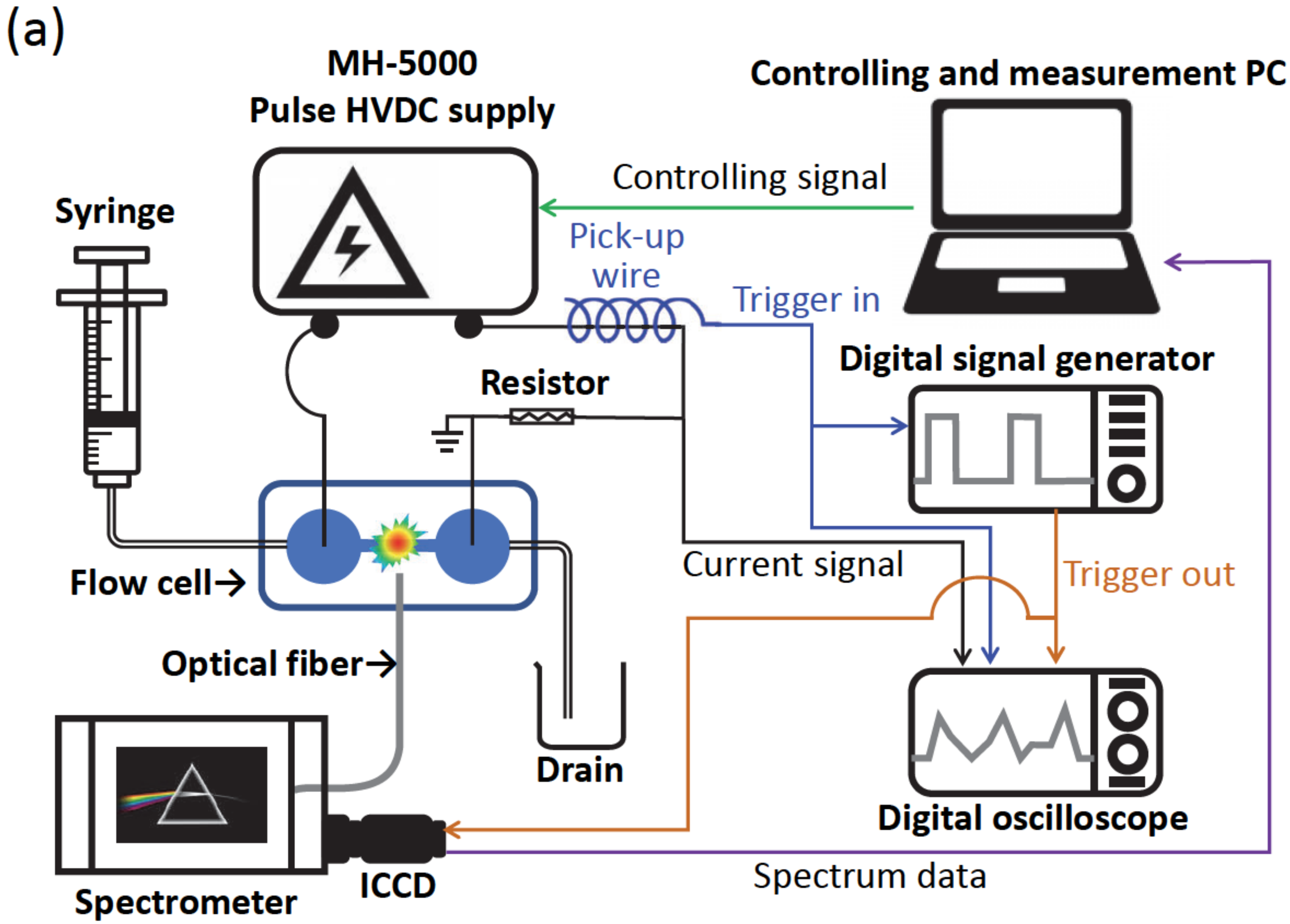
(a)
MH-5000
Pulse HVDC supply
Controlling and measurement PC
Controlling signal
Syringe
Pick-up
wire
Trigger in
Digital signal generator
Resistor
Flow cell→
Current signal
Trigger out
Optical fiber→
Drain
Digital oscilloscope
Spectrometer
ICCD
Spectrum data

Figure 1b

(b)

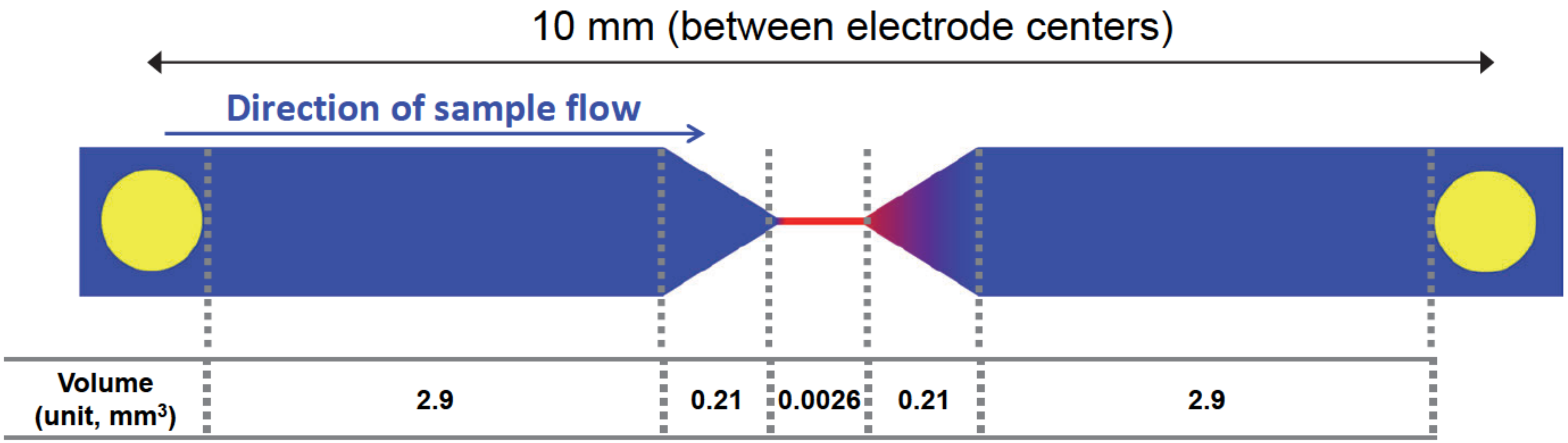

Volume (unit, mm^3)	2.9	0.21	0.0026	0.21	2.9

Yellow zone, electrodes; blue zone, sample solution; red zone, LEP capillary.

Figure 2

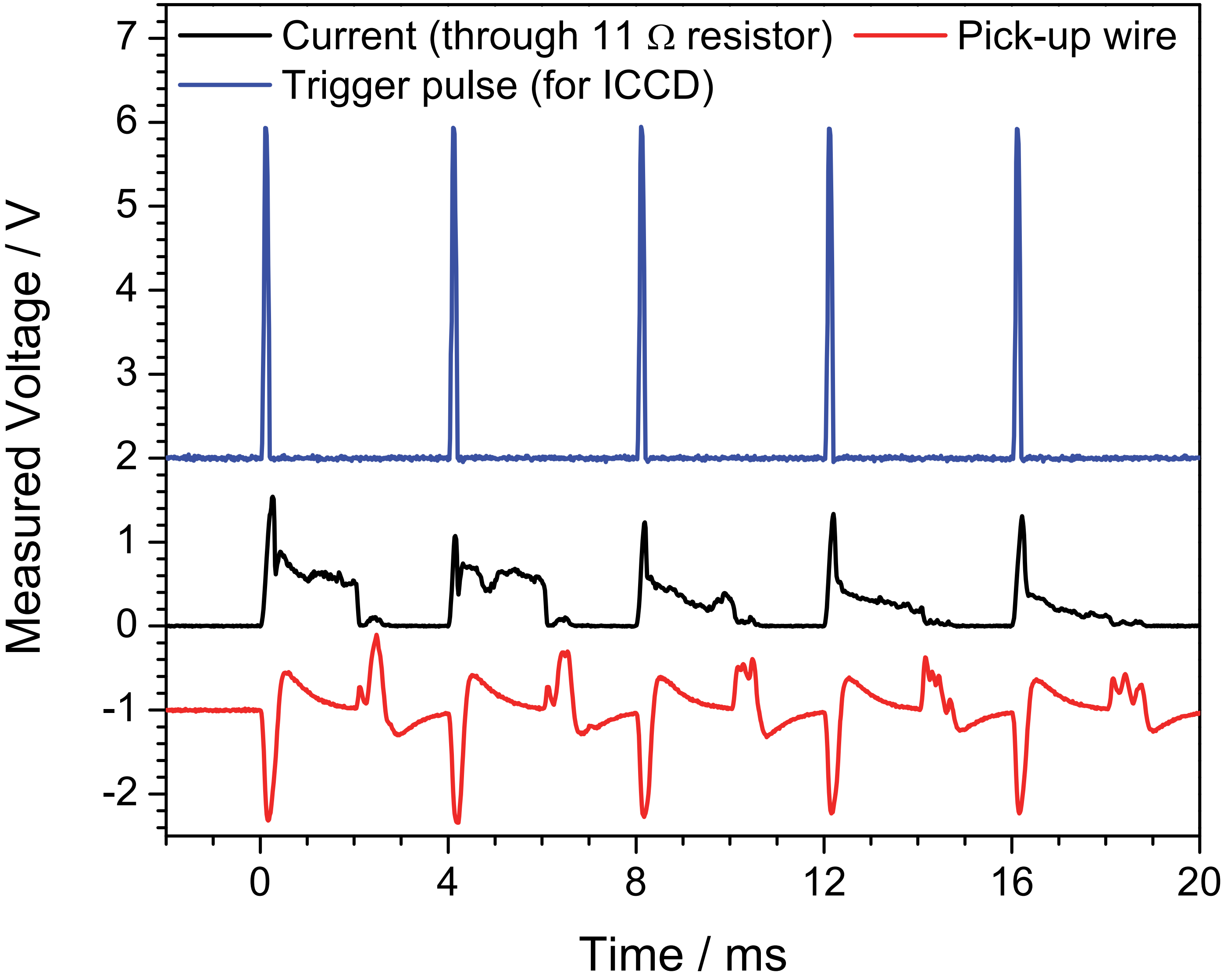

Current (through 11 Ω resistor)
Pick-up wire
Trigger pulse (for ICCD)
Measured Voltage / V
7
6
5
4
3
2
1
0
-1
-2
Time / ms
0
4
8
12
16
20

Figure 3

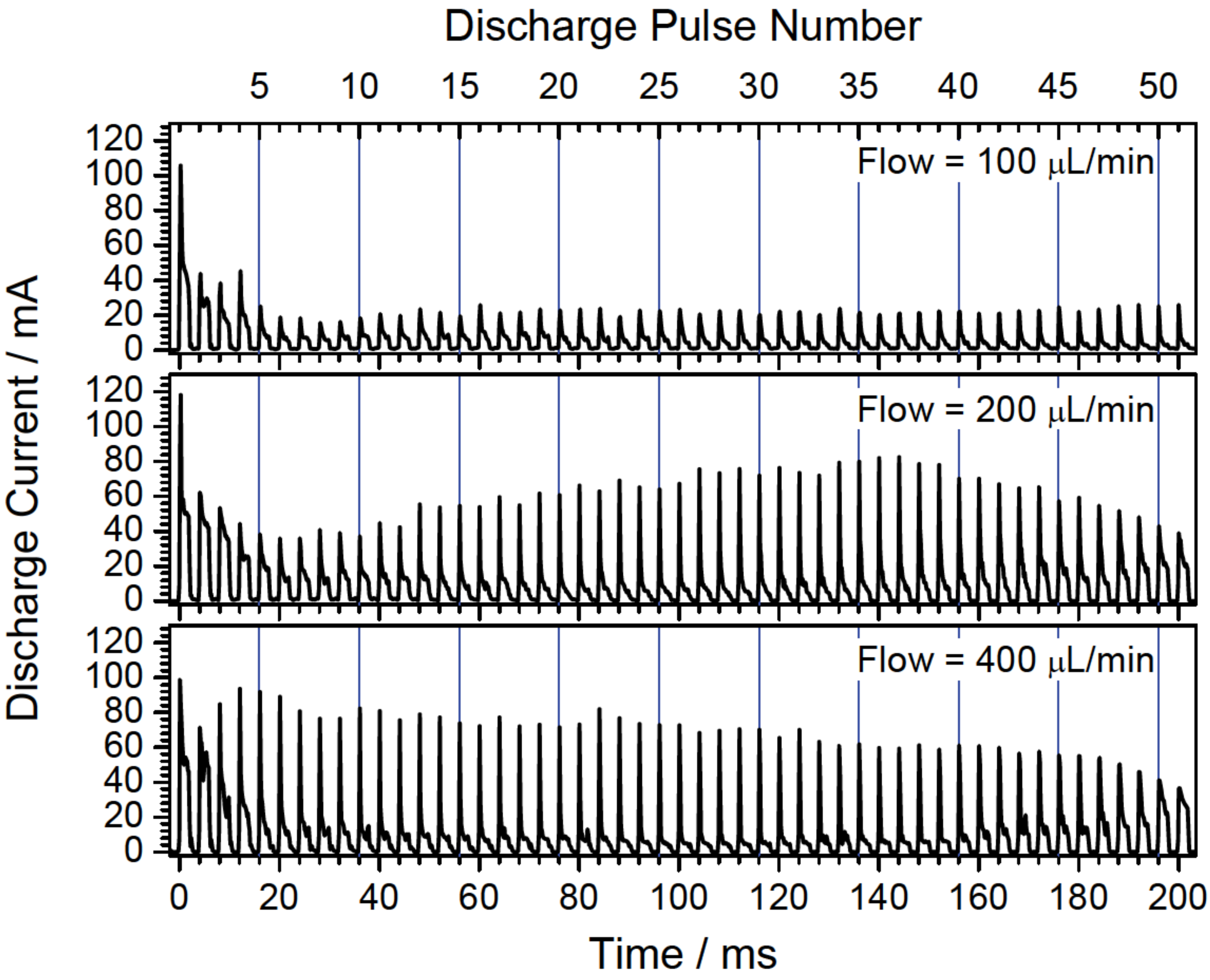
Discharge Pulse Number
5
10
15
20
25
30
35
40
45
50
Flow = 100 μL/min
Flow = 200 μL/min
Flow = 400 μL/min
Discharge Current / mA
0
20
40
60
80
100
120
Time / ms
0
20
40
60
80
100
120
140
160
180
200

Figure 4

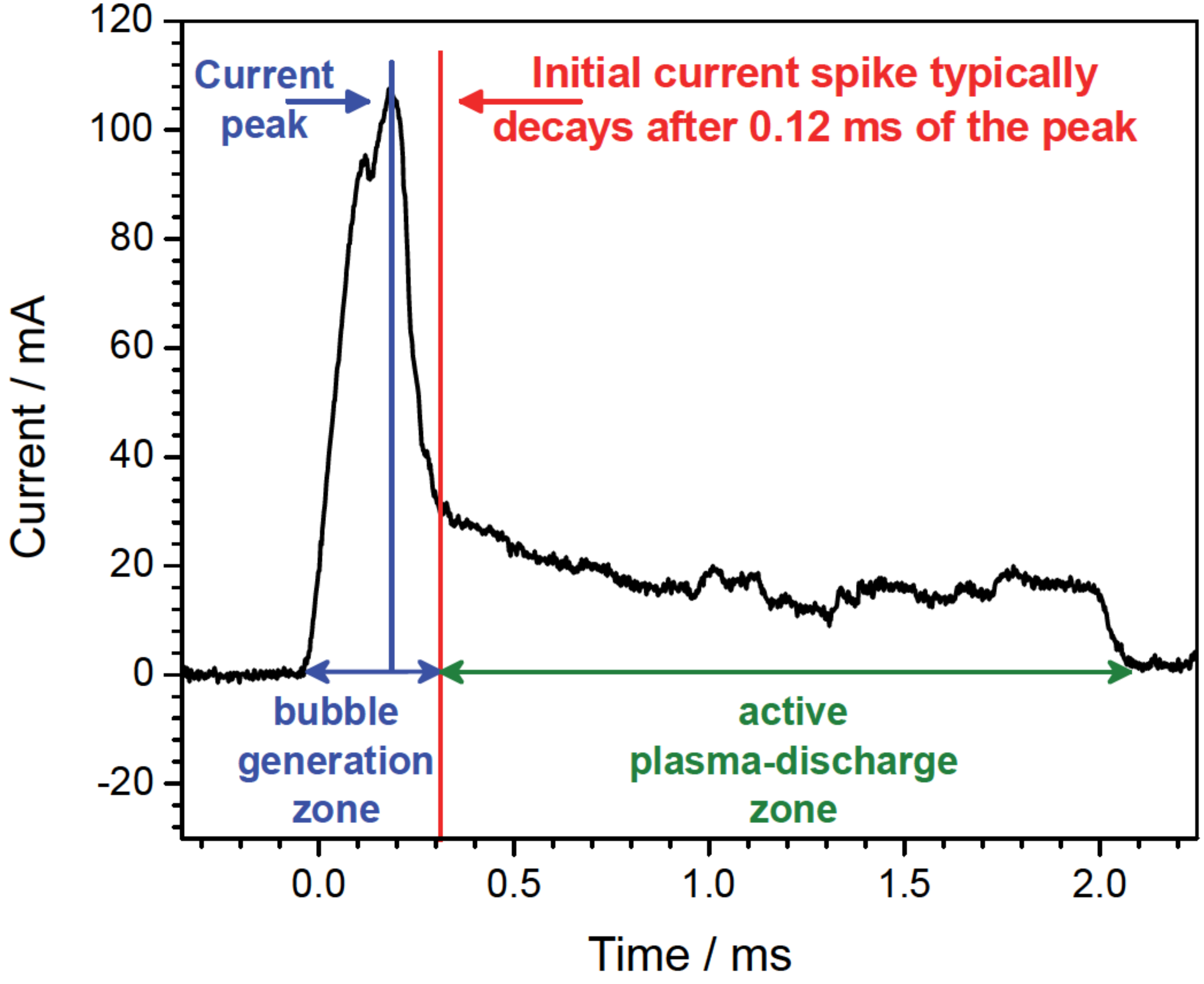

Current peak
Initial current spike typically decays after 0.12 ms of the peak
bubble generation zone
active plasma-discharge zone
120
100
80
60
40
20
0
-20
Current / mA
0.0
0.5
1.0
1.5
2.0
Time / ms

Figure 5

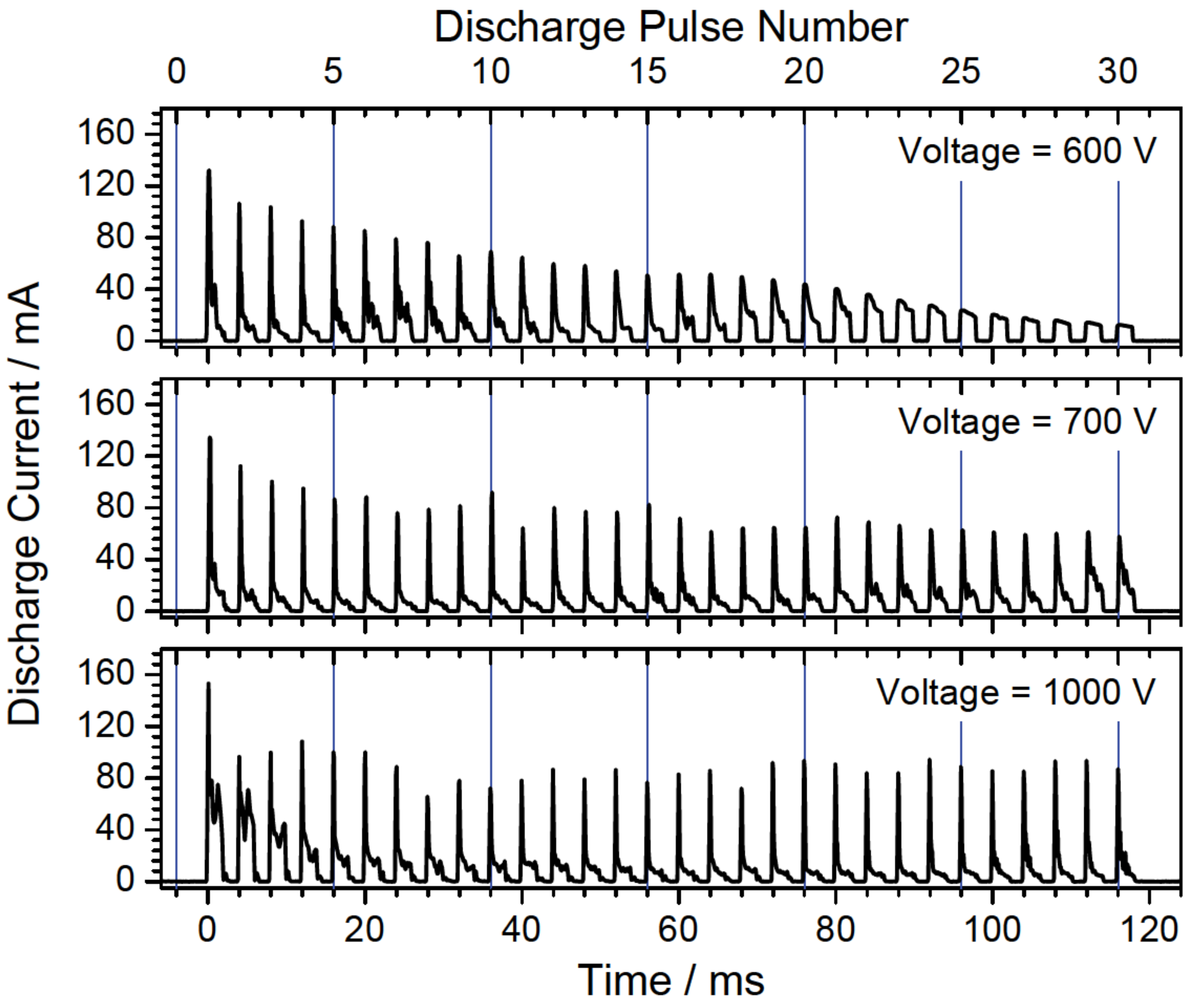
Discharge Pulse Number
0
5
10
15
20
25
30
Voltage = 600 V
Voltage = 700 V
Voltage = 1000 V
Discharge Current / mA
160
120
80
40
0
Time / ms
0
20
40
60
80
100
120

Figure 6a

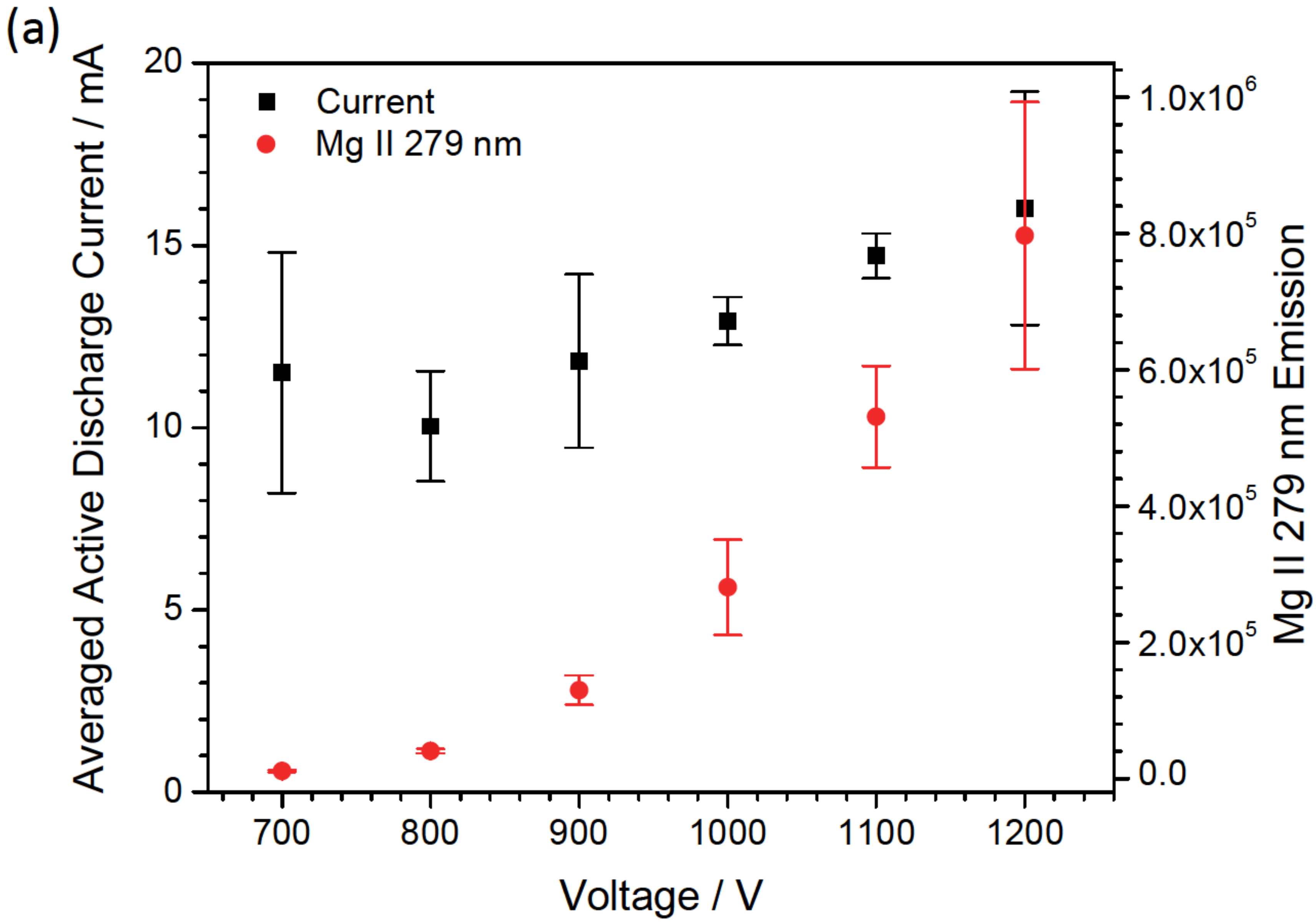
(a)
Current
Mg II 279 nm
Averaged Active Discharge Current / mA
0
5
10
15
20
Mg II 279 nm Emission
0.0
2.0x10^5
4.0x10^5
6.0x10^5
8.0x10^5
1.0x10^6
700
800
900
1000
1100
1200
Voltage / V

Figure 6b

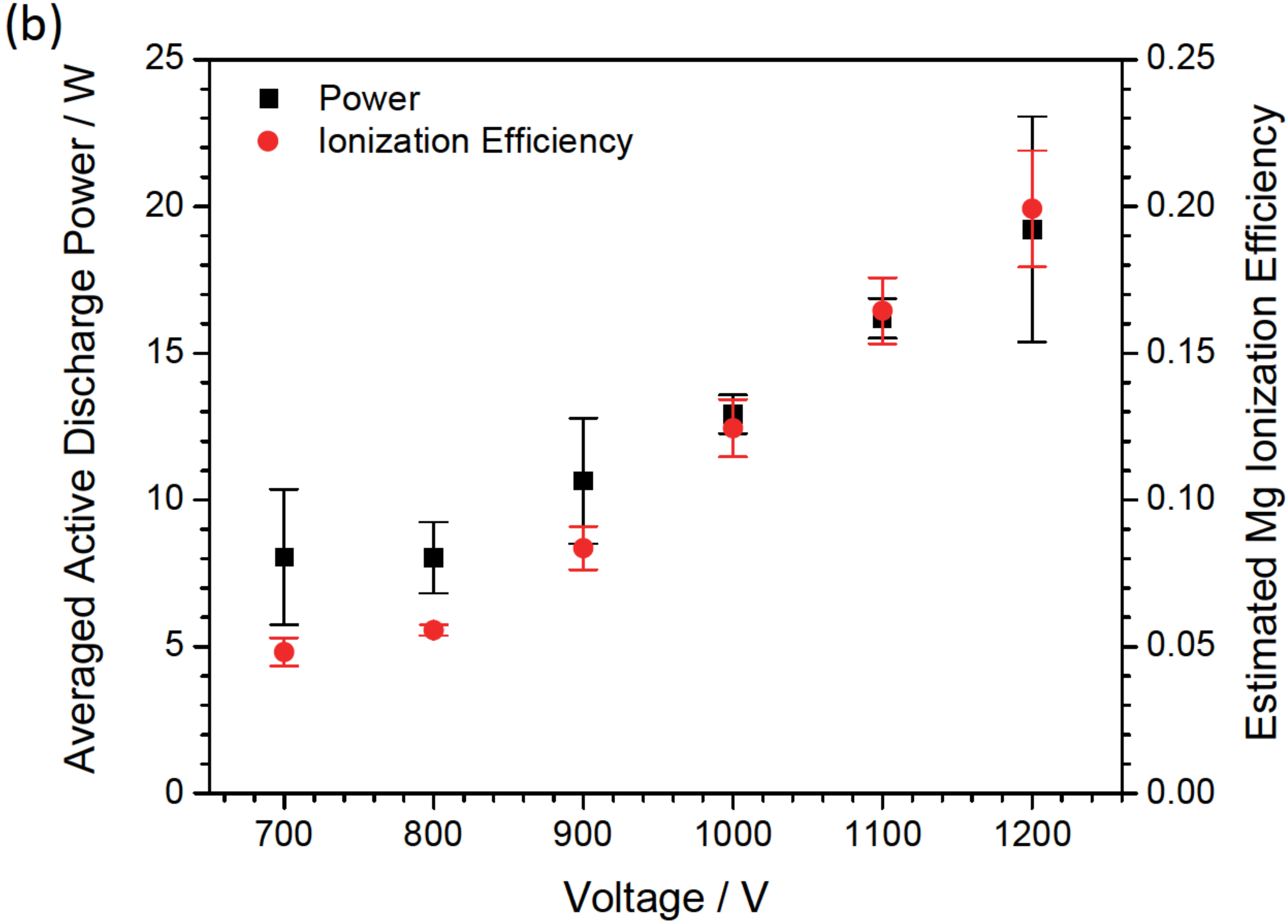
(b)
Power
Ionization Efficiency
Averaged Active Discharge Power / W
25
20
15
10
5
0
700
800
900
1000
1100
1200
Voltage / V
Estimated Mg Ionization Efficiency
0.25
0.20
0.15
0.10
0.05
0.00

Figure 7a

(a)

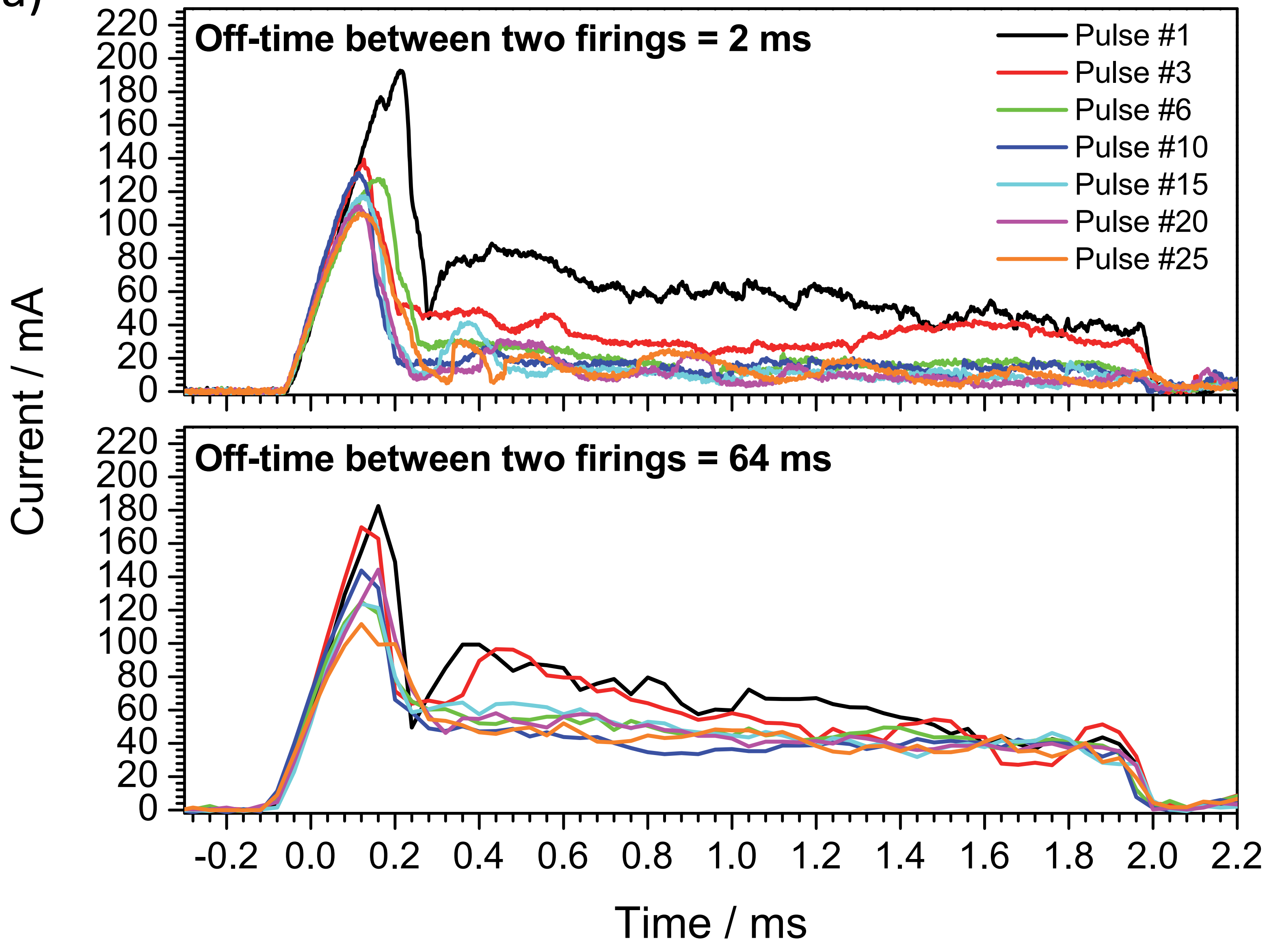
Off-time between two firings = 2 ms
Off-time between two firings = 64 ms
Pulse #1
Pulse #3
Pulse #6
Pulse #10
Pulse #15
Pulse #20
Pulse #25
Current / mA
Time / ms
0
20
40
60
80
100
120
140
160
180
200
220
-0.2
0.0
0.2
0.4
0.6
0.8
1.0
1.2
1.4
1.6
1.8
2.0
2.2

Figure 7b

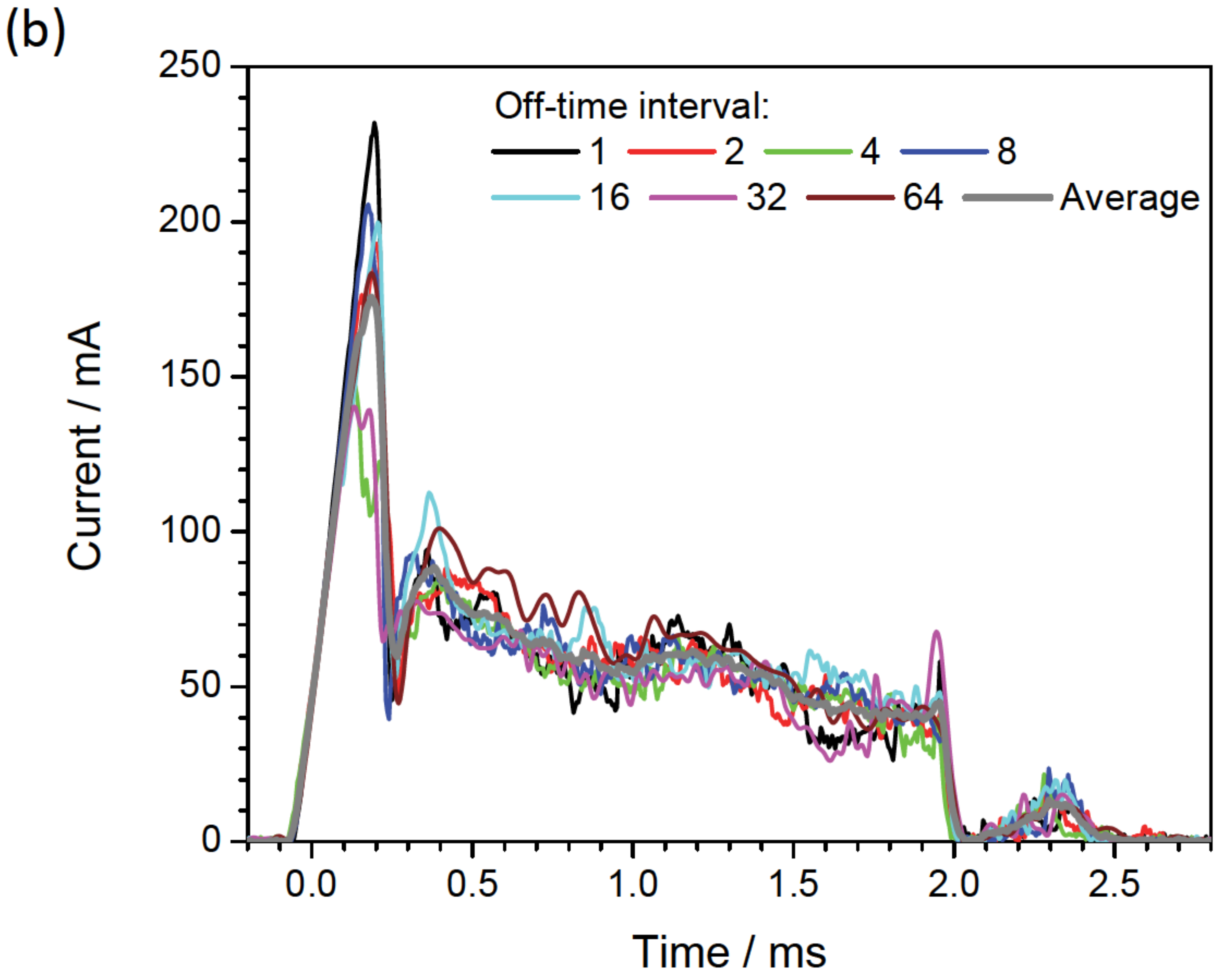
(b)
Off-time interval:
1
2
4
8
16
32
64
Average
Current / mA
250
200
150
100
50
0
0.0
0.5
1.0
1.5
2.0
2.5
Time / ms

Figure 7c

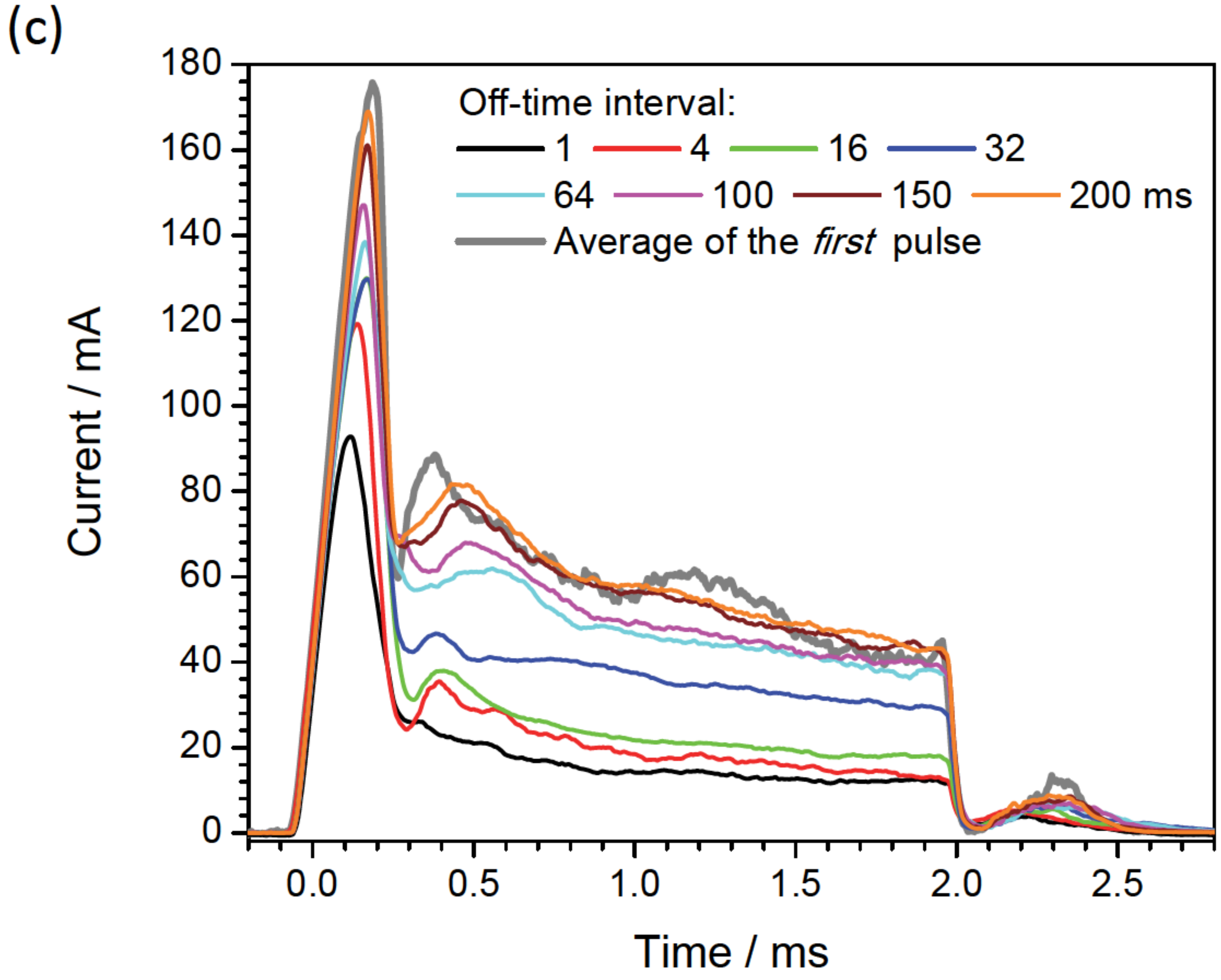
(c)
Current / mA
Time / ms
180
160
140
120
100
80
60
40
20
0
0.0
0.5
1.0
1.5
2.0
2.5
Off-time interval:
1
4
16
32
64
100
150
200 ms
Average of the *first* pulse

Figure 8a

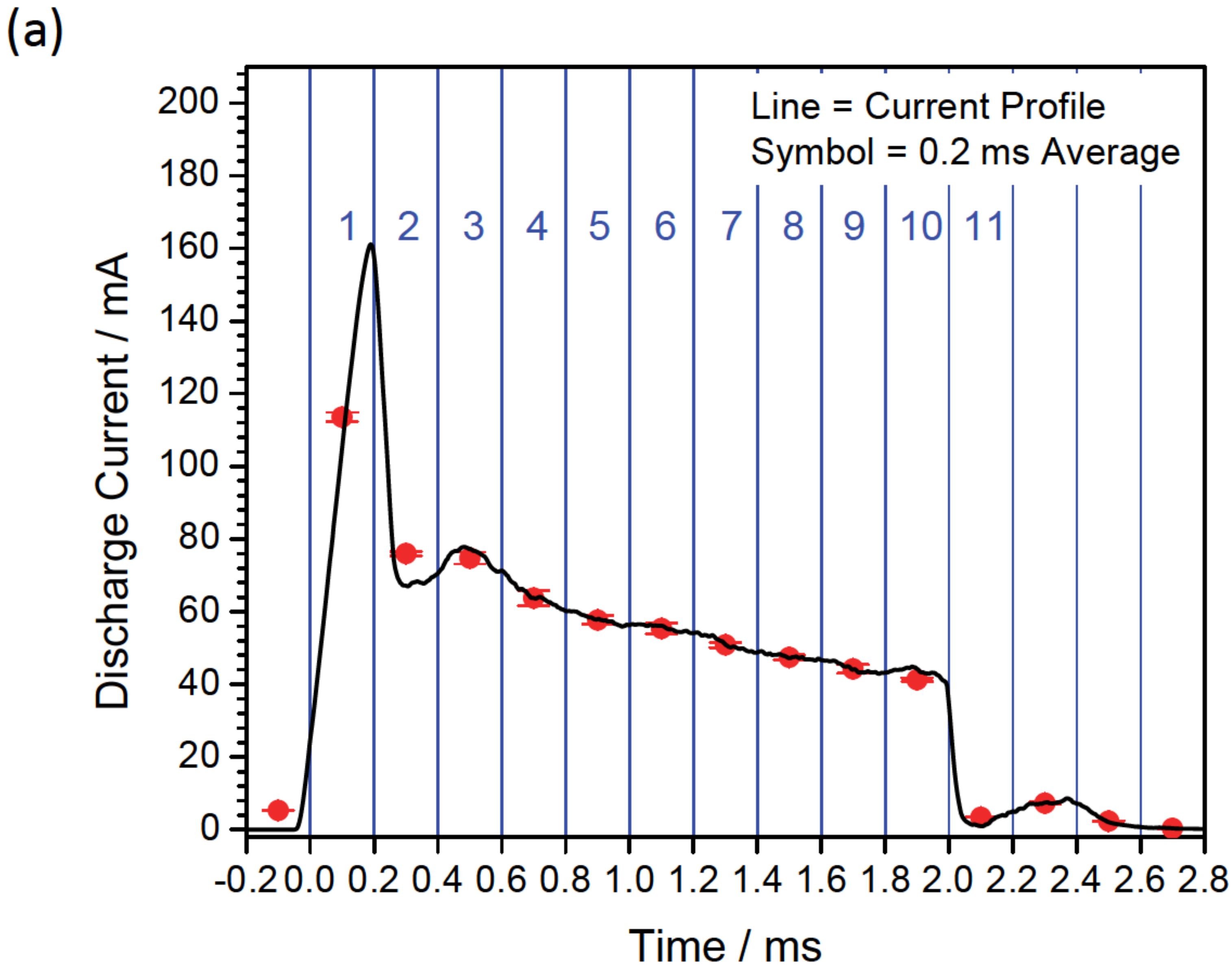
(a)
Line = Current Profile
Symbol = 0.2 ms Average
1
2
3
4
5
6
7
8
9
10
11
Discharge Current / mA
0
20
40
60
80
100
120
140
160
180
200
-0.2
0.0
0.2
0.4
0.6
0.8
1.0
1.2
1.4
1.6
1.8
2.0
2.2
2.4
2.6
2.8
Time / ms

Figure 8b

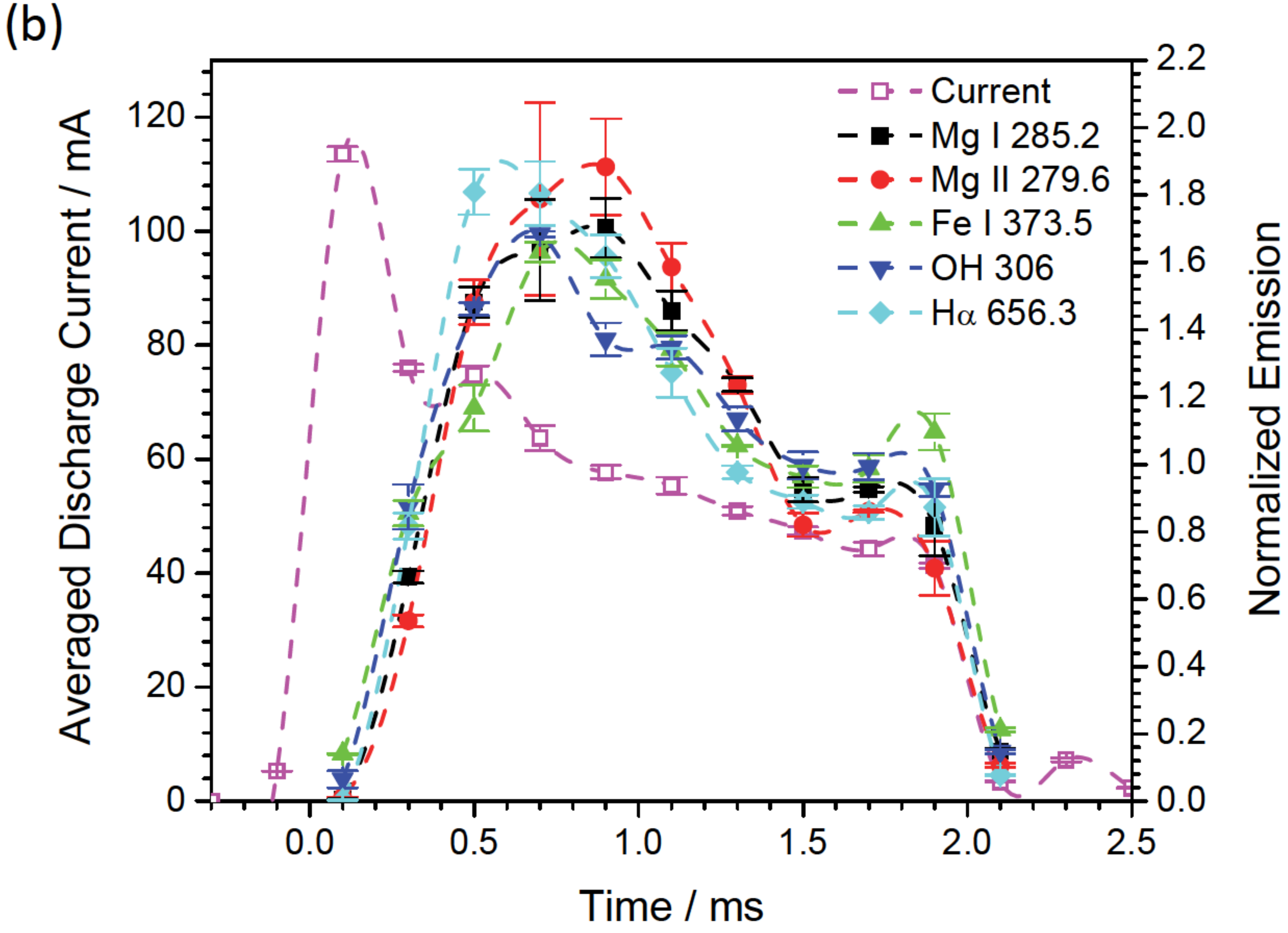
(b)
Averaged Discharge Current / mA
Normalized Emission
Time / ms
Current
Mg I 285.2
Mg II 279.6
Fe I 373.5
OH 306
Hα 656.3
0
20
40
60
80
100
120
0.0
0.2
0.4
0.6
0.8
1.0
1.2
1.4
1.6
1.8
2.0
2.2
0.0
0.5
1.0
1.5
2.0
2.5

Figure 9

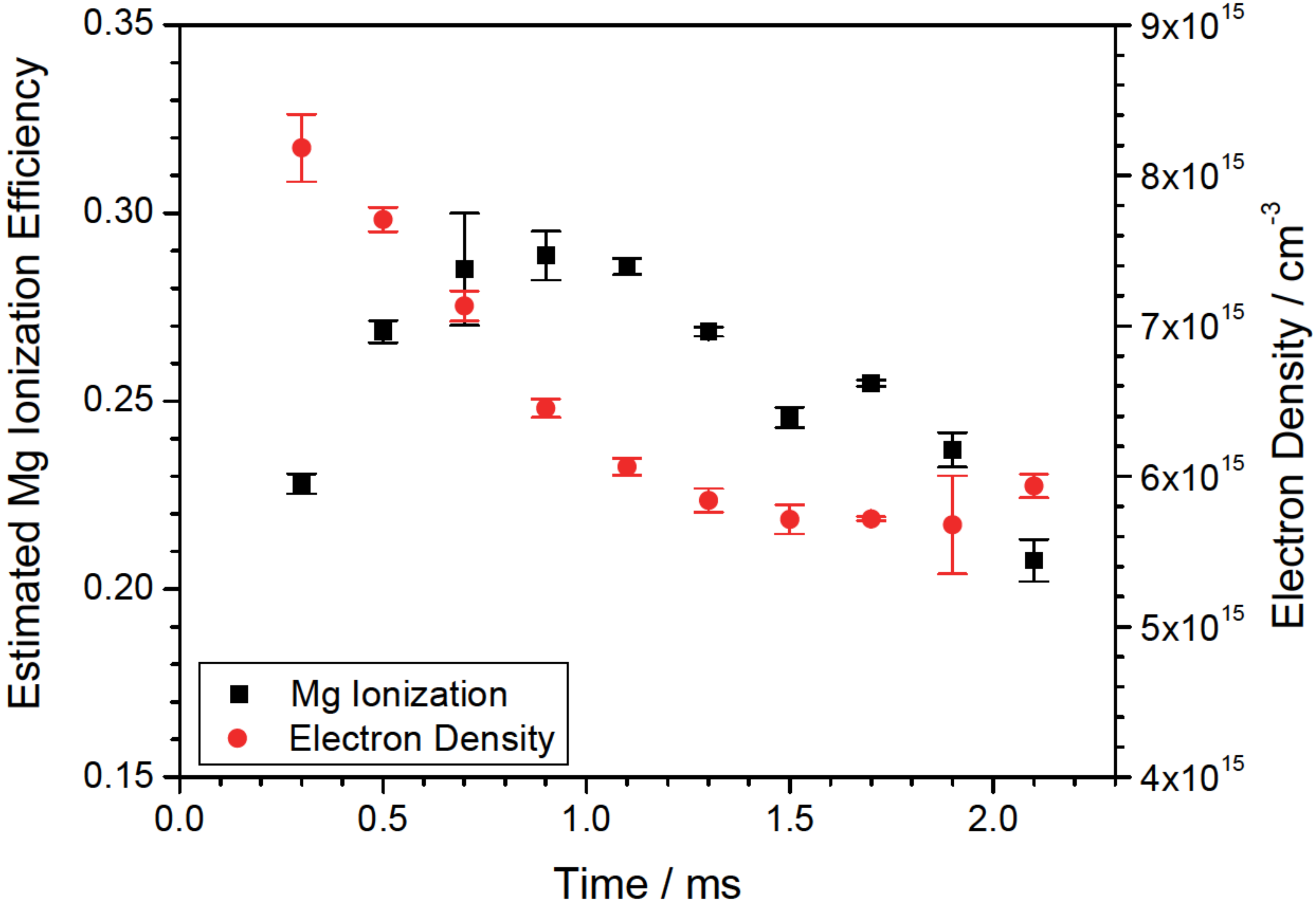
Estimated Mg Ionization Efficiency
0.35
0.30
0.25
0.20
0.15
0.0
0.5
1.0
1.5
2.0
Time / ms
$9x10^{15}$
$8x10^{15}$
$7x10^{15}$
$6x10^{15}$
$5x10^{15}$
$4x10^{15}$
Electron Density / cm^{-3}
■ Mg Ionization
● Electron Density

Figure 10a

(a)

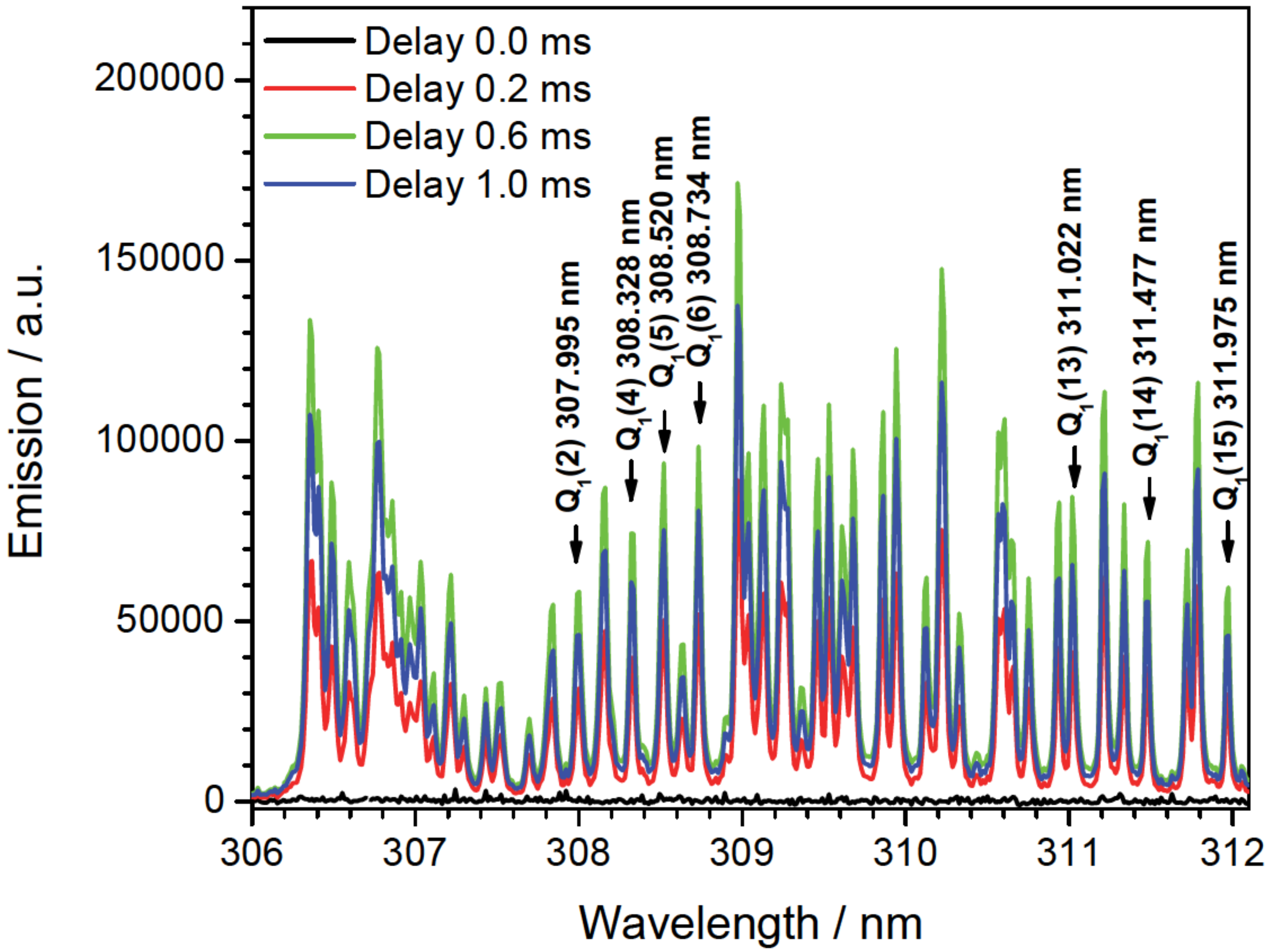

Delay 0.0 ms
Delay 0.2 ms
Delay 0.6 ms
Delay 1.0 ms
$Q_1(2)$ 307.995 nm
$Q_1(4)$ 308.328 nm
$Q_1(5)$ 308.520 nm
$Q_1(6)$ 308.734 nm
$Q_1(13)$ 311.022 nm
$Q_1(14)$ 311.477 nm
$Q_1(15)$ 311.975 nm
Emission / a.u.
0
50000
100000
150000
200000
306
307
308
309
310
311
312
Wavelength / nm

Figure 10b

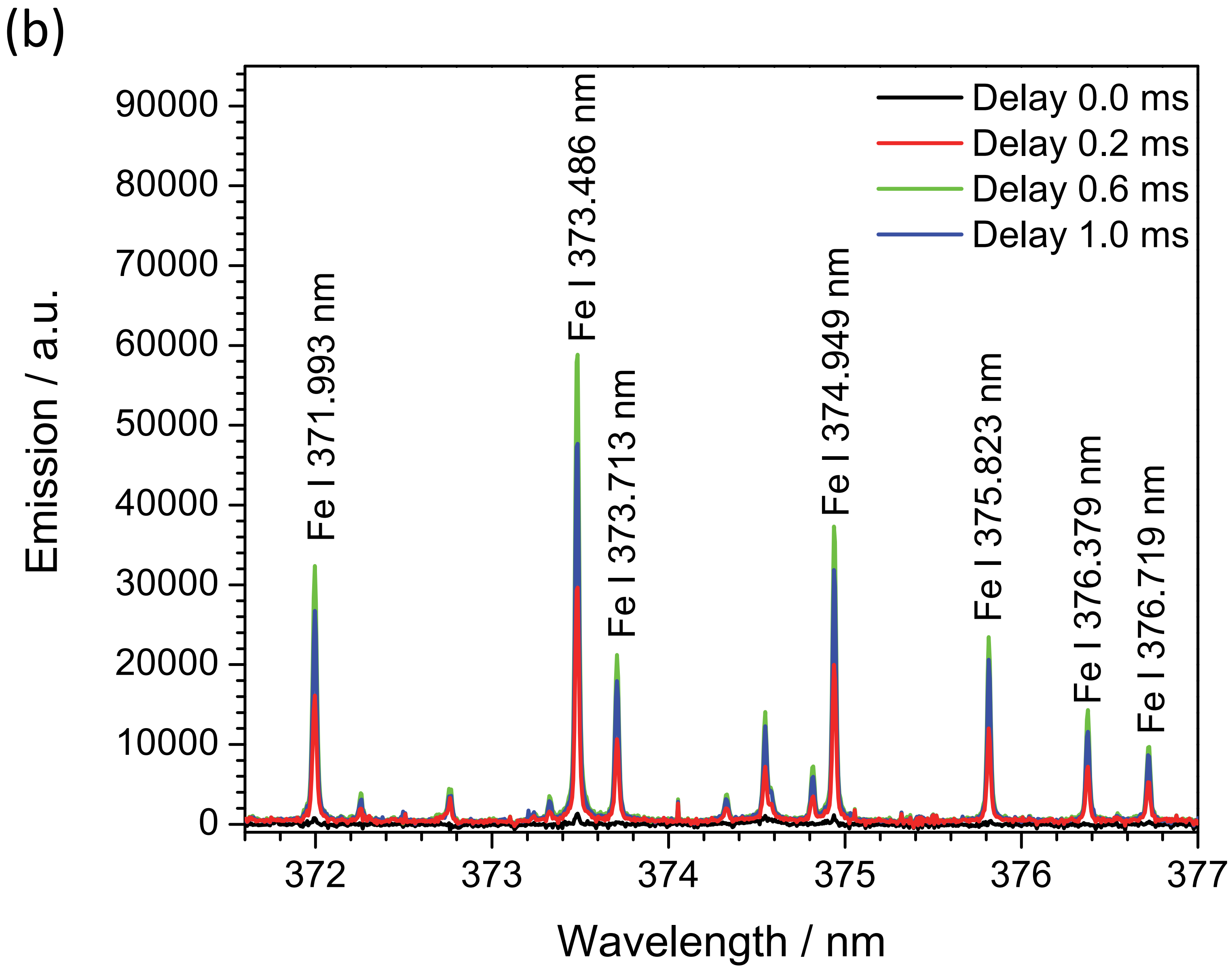
(b)
Emission / a.u.
90000
80000
70000
60000
50000
40000
30000
20000
10000
0
372
373
374
375
376
377
Wavelength / nm
Delay 0.0 ms
Delay 0.2 ms
Delay 0.6 ms
Delay 1.0 ms
Fe I 371.993 nm
Fe I 373.486 nm
Fe I 373.713 nm
Fe I 374.949 nm
Fe I 375.823 nm
Fe I 376.379 nm
Fe I 376.719 nm

Figure 11

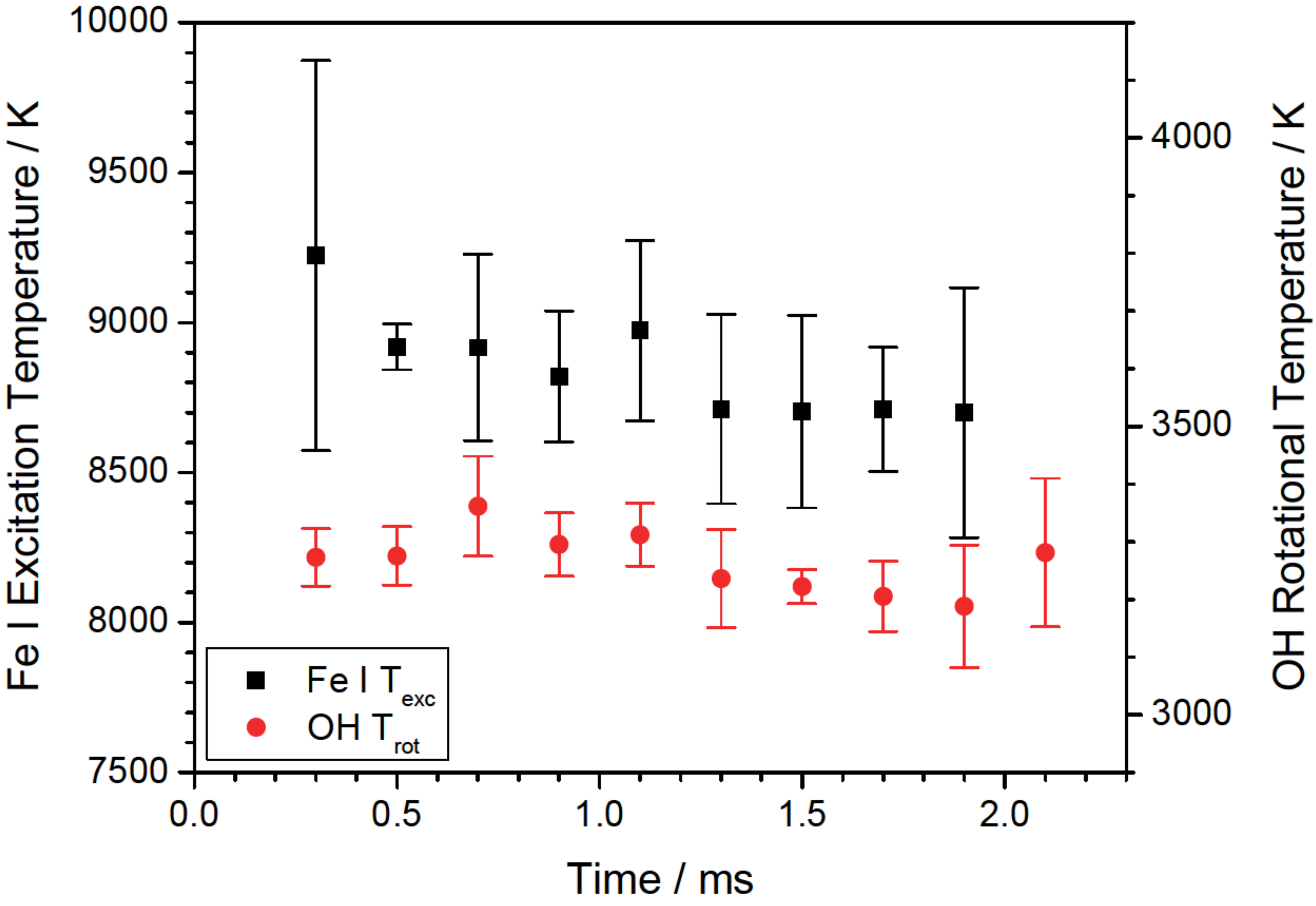
Fe I Excitation Temperature / K
10000
9500
9000
8500
8000
7500
OH Rotational Temperature / K
4000
3500
3000
0.0
0.5
1.0
1.5
2.0
Time / ms
■ Fe I T_{exc}
● OH T_{rot}